

1 **The influence of multiple groups of biological ice nucleating particles on microphysical**
2 **properties of mixed-phase clouds observed during MC3E**

3
4
5 Sachin Patade^{1*}, Deepak Waman¹, Akash Deshmukh¹, Ashok Kumar Gupta², Arti Jadav¹,
6 Vaughan T. J. Phillips¹, Aaron Bansemer⁴, Jacob Carlin³, Alexander Ryzhkov³,

7
8 ¹Department of Physical Geography and Ecosystem Science, Lund University, Lund, Sweden

9 ²Department of Earth and Environmental Sciences, Vanderbilt University, Nashville, TN,
10 37240, USA

11 ³Cooperative Institute for Severe and High-Impact Weather Research and Operations, The
12 University of Oklahoma, and NOAA/OAR National Severe Storms Laboratory, Norman,
13 Oklahoma, USA

14 ⁴National Center for Atmospheric Research, Boulder, Colorado, USA

15
16
17
18
19
20
21
22
23
24 *** Corresponding Author**

25 **Dr. Sachin Patade, Lund University, Sweden**

26 **email: sachin.patade@nateko.lu.se**

31 **Abstract:**

32 A new empirical parameterization (EP) for multiple groups of primary biological aerosol
33 particles (PBAPs) is implemented in the aerosol-cloud model (AC) to investigate their roles
34 as ice-nucleating particles (INPs). The EP describes the heterogeneous ice nucleation by (1)
35 fungal spores, (2) bacteria, (3) pollen, (4) detritus of plants, animals, and viruses, and (5)
36 algae. Each group includes fragments from the originally emitted particles. A high-resolution
37 simulation of a midlatitude mesoscale squall line by AC is validated against airborne and
38 ground observations.

39

40 Sensitivity tests are carried out by varying the initial vertical profiles of the loadings of
41 individual PBAP groups. The resulting changes in warm and ice cloud microphysical
42 parameters are investigated. The changes in warm microphysical parameters including liquid
43 water content, and cloud droplet number concentration are minimal ($< 10\%$). Overall, PBAPs
44 have little effect on ice number concentration ($< 6\%$) in the convective region. In the
45 stratiform region, increasing the initial PBAP loadings by a factor of 1000 resulted in less
46 than 40% change in ice number concentrations. The total ice concentration is mostly
47 controlled by various mechanisms of secondary ice production (SIP). However, when SIP is
48 intentionally shut down in sensitivity tests, increasing the PBAP loading by a factor of 100
49 has less than a 3% effect on the ice phase. Further sensitivity tests revealed that PBAPs have
50 little effect on surface precipitation as well as on shortwave and longwave flux ($< 4\%$) for
51 100-fold perturbation in PBAPs.

52

53

54

55 **1. Introduction**

56 In most climate models, the largest source of uncertainty for estimating the total
57 anthropogenic forcing is associated with cloud-aerosol interactions (Pörtner et al., 2022).
58 Atmospheric aerosol particles can act as cloud condensation nuclei (CCN) and a few of them
59 act as ice-nucleating particles (INPs), thereby influencing the microphysical properties of
60 clouds and, depending on the cloud type (Fan et al. 2010; Chen et al 2019). The treatment of
61 INP in climate models can strongly affect the atmospheric radiation budget (DeMott et al.
62 2010). Various sources of aerosol particles, including dust/metallic, marine aerosols,
63 anthropogenic carbonaceous emissions, and primary biological aerosol particles (PBAPs),
64 contribute to the observed INPs (Kanji et al. 2017).

65

66 A significant amount of global precipitation is associated with the ice phase in cold clouds
67 (Heymsfield and Field 2015; Mülmenstädt et al. 2015, Heymsfield et al. 2020). In particular,
68 mixed-phase clouds are vital for the global climate (Dong and Mace 2003; Zuidema et al.
69 2005; Matus and L'Ecuyer 2017; Korolev et al. 2017 and references therein). In a multimodel
70 simulation study, Tsushima et al. (2006) showed that the doubling of CO₂ concentrations
71 caused the changes in the distribution of cloud-water in the mixed-phase clouds in a climate
72 simulation to be significant.

73

74 PBAPs are solid particles of biological origin and are emitted from the Earth's surface
75 (Després et al. 2012). They are highly active in initiating ice as INPs and include bacteria,
76 fungal spores, pollen, algae, lichens, archaea, viruses, and biological fragments (e.g., leaf
77 litters, insects) and molecules (e.g., proteins, polysaccharides, lipids) (Després et al., 2012;
78 Fröhlich-Nowoisky et al., 2015; Knopf et al., 2011; Szyrmer and Zawadzki, 1997;).

79 Considering the onset temperature of freezing, some ice nucleation active fungi and bacteria
80 (especially *Pseudomonas syringae* with onset freezing temperature around -3°C) are among
81 the most active INPs present in the atmosphere (Després et al. 2012; Hoose and Möhler
82 2012). The potential impact of PBAP INPs on cloud microphysical characteristics has been
83 recognized for many years; however, this topic remains a subject of debate (DeMott and
84 Prenni 2010; Spracklen and Herald, 2014; Hoose et al. 2010b). Some previous modeling
85 studies have shown that on a global scale PBAPs have only a limited influence on clouds and
86 precipitation (Hoose et al. 2010; Sesartic et al. 2012, 2013; Spracklen and Heald 2014). On a
87 global scale, the percentage contribution of PBAPs to the immersion freezing (ice nucleation
88 by INP immersed in supercooled water drop) is predicted to be much smaller (0.6%) as
89 compared to dust (87%) and soot (12%) (Hoose et al. 2010).

90

91 Many studies have used cloud models to highlight the potential impact of PBAP INPs on
92 cloud microphysics and precipitation (e.g., Levin et al. 1987; Grützun et al. 2008; Phillips et
93 al. 2009). For example, the mesoscale aerosol-cloud model by Phillips et al. (2009) had a 3-D
94 domain of about 100 km in width, and many cloud types were present in the mesoscale
95 convective system that was simulated. Their simulations revealed that the cloud cover,
96 domain radiative fluxes, and surface precipitation rate were significantly altered by boosting
97 organic aerosols representing PBAPs. According to Hummel et al. (2018) in shallow mixed-
98 phase clouds (i.e., altostratus) when the cloud top temperature is below -15°C , PBAPs have
99 the potential to influence the cloud ice phase and produce ice crystals in the absence of other
100 INPs.

101

102 The quest for insights into the broader atmospheric role of PBAP INPs for cloud
103 microphysical properties and precipitation is hampered by the limited availability of
104 observations both of their ice nucleation activities for various species and their aerosol
105 distributions in the real atmosphere (Huang et al. 2021). More generally, there is incomplete
106 knowledge about the chemical identity of the key INPs, whether biological or otherwise
107 (Murray et al. 2012). In many global and regional models, the ice nucleation activity of
108 bioaerosols is represented either empirically or theoretically based on laboratory
109 measurements of specific biological species of PBAPs that are assumed as representative
110 candidates (e.g., *Pseudomonas syringae*). This assumption of representativeness introduces
111 uncertainties that would be expected to impact the model results, potentially introducing a
112 bias into the estimation of the effects of bioaerosols on clouds (e.g. Sahyoun et al., 2016;
113 Hoose et al. 2010b; Spracklen and Herald, 2014, Huang et al. 2021 and references therein).

114

115 In addition to primary ice nucleation, ice formation in clouds can occur because of processes
116 generating new particles from pre-existing ice, and these are known as Secondary Ice
117 Production (SIP) mechanisms (Korolev and Leisner, 2020; Korolev et al, 2020). SIP can have
118 a considerable impact on cloud micro- and macro-physical properties such as precipitation
119 rate, glaciation time, cloud lifetime, and cloud electrification by increasing the ice number
120 concentrations by a few orders of magnitude (e.g., Blyth and Latham 1993; Crawford et al.,
121 2012; Lawson et al., 2015; Phillips et al., 2017b, 2018, 2020; Phillips and Patade, 2021;
122 Sotiropoulou et al. 2021a,b). This in turn can influence the global hydrological cycle and
123 climate. For example, Zhao and Liu (2021) demonstrated using a global climate model that
124 SIP dominates ice formation in moderately cold clouds and has a significant influence on
125 their liquid and ice water paths. They showed that including three SIP mechanisms in the
126 model simulated global annual average liquid water path decreases by 15 g m^{-2} (-22%

127 change) and the ice water path increases by 9 g m^{-2} (23%), resulting in better agreement with
128 observations. Accounting for SIP in their model results in a change in the global annual
129 average net cloud radiative forcing by about 1 W m^{-2} . Although a small fraction of the total
130 cloud radiative forcing globally, this flux change underlines the ubiquitous role of SIP on
131 cloud properties on the large scale.

132

133 However, in many cloud models, the representations of these SIP mechanisms are uncertain
134 as most of the cloud models include only the Hallett-Mossop (hereafter HM; Hallett and
135 Mossop, 1974) process and neglect other SIP mechanisms (e.g. Fan et 2017; Han et al 2019).
136 A few secondary ice formation processes (e.g., the HM process) have been suggested to be
137 active in the temperature range where active PBAP INPs exhibit strong ice nucleation
138 activity. The INPs of biological origin such as bacteria are highly active in the temperature
139 range of the HM process (-3 to -8°C) as compared with non-biological INPs (Möhler et al.
140 2008; Patade et al., 2021, henceforth PT21). At temperatures warmer than -15°C , some of the
141 PBAPs generated by biologically active landscapes (e.g. forests, woodlands) can promote ice
142 formation and crystal growth in clouds (Morris et al., 2014).

143

144 In the USA, about 18% of the total landmass is used as cropland, farmland, and agricultural
145 activities (Garcia et al. 2012). These are major sources of biological particles in the
146 atmosphere. Biogenic particles released from crops, either pre- and post-harvest, have
147 previously been shown to serve as INPs (in Colorado and Nebraska, Garcia et al. 2012).
148 Huffman et al. (2013) found that airborne biological particles increase significantly in
149 concentration, by an order of magnitude or more, during rainfall in a forest in the western US
150 and that bioaerosols are well correlated with INPs. Prenni et al. (2013) observed a similar

151 increase in concentrations of ground-level INPs during rain at a forested site in Colorado,
152 which was associated with increased biological particles. If these potential INPs are detrained
153 from the convective outflow of a cell at mid-levels, then they may be entrained into other
154 clouds aloft, influencing the microphysical properties of that subsequent storm. Convective
155 clouds can efficiently transport lower tropospheric aerosol particles into the upper
156 troposphere where they can affect the cloud properties (Cui and Carslaw, 2006)

157

158 The current study aims to simulate realistic concentrations of multiple groups of PBAP INPs,
159 including bacterial and fungal particles, to investigate their interactions with convective
160 clouds observed during the Midlatitude Continental Convective Clouds Experiment field
161 campaign (MC3E), in the USA (Jensen et al. 2016), in the USA. In view of the literature
162 noted above about the effects of PBAP INPs, there is a need for more detailed analyses of
163 their role in altering cloud microphysical properties and precipitation because the realistic
164 treatment of ice nucleation activity for major PBAP groups was not available, prior to our
165 empirical scheme (PT21). Hitherto, laboratory measurements of isolated biological species
166 (e.g., *Pseudomonas syringae*, *Cladosporium sp*) have been the basis for attempts to simulate
167 biological ice nucleation in clouds, but the representativeness of the choice of such species
168 has been a longstanding issue. For example, Hummel et al (2018) considered three highly ice-
169 nucleation-active PBAP species in their model which may not represent the ice nucleation
170 activity of PBAP in the atmosphere. It is not known which biological species of ice
171 nucleation active (INA) PBAPs contribute the most to biological ice nucleation.
172 Consequently, there is a need for a new approach oriented toward laboratory measurements
173 of biological INPs sampled from the atmosphere, thus optimizing the representativeness of
174 the data for studies of clouds.

175

176 In this paper, such an approach is followed to investigate the effect on cloud properties from
177 various major groups of PBAP. We incorporated a recent empirical parameterization for
178 various PBAP groups by PT21 into our 3D aerosol-cloud model (AC). PT21 created an
179 empirical formulation resolving the ice nucleation of each group of PBAPs including 1)
180 fungal spores and their fragments, 2) bacteria and their fragments, 3) pollen and their
181 fragments, 4) detritus of plants, animals, and viruses, and 5) algae. The empirical formulation
182 by PT21 is based on observations of PBAP collected at the Amazon Tall Tower Observatory
183 (ATTO). It is a research site located in the middle of the Amazon rainforest in northern
184 Brazil. In this article, we also examine the relative importance of various secondary ice
185 processes in their role in mediating the PBAP effects on cloud microphysical properties,
186 given the weakness of PBAP effects on cloud microphysical properties.

187

188

189 **2. Description of observations**

190 *2.1 Selected case of a deep convective system*

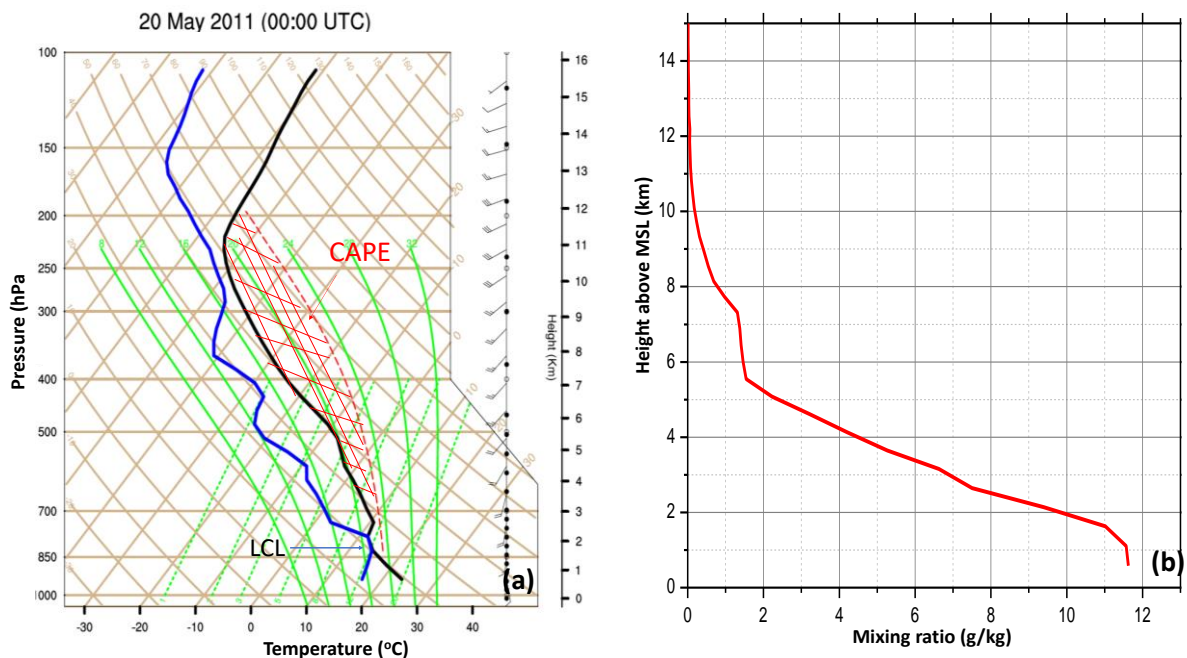
191 In the current study, we simulated a squall line that occurred on 20 May 2011 MC3E
192 (Jensen et al. 2016). The MC3E campaign took place from 22 April through to 6 June 2011
193 and was centered at the Atmospheric Radiation Measurement (ARM) Southern Great Plains
194 (SGP) Central Facility (CF), (36.6°N, 97.5°W) in north-central Oklahoma. Jensen et al.
195 (2016) describe the squall line as a "golden event" of the MC3E campaign given the robust *in*
196 *situ* sampling of extensive stratiform outflow from deep convection on this day. The surface
197 meteorological analysis on 20 May indicated a southerly flow at the surface, which provided
198 enough moisture from the Gulf of Mexico to trigger convection. Deep convection, organized

199 in the form of a squall line, passed over the measurement site between 1030 and 1100 UTC,
200 resulting in convective precipitation. It was followed by widespread stratiform precipitation
201 that was well observed by both airborne and ground-based measurements.

202

203 The skew- T plot from the radiosonde sounding conducted on 20 May 2011, at (00 UTC) is
204 shown in Figure 1a. The skew- T plot shows the vertical sounding before the formation of
205 deep convection. The skew- T plot shows that the surface-based Convective Available
206 Potential Energy (CAPE) for this case was 2400 J kg^{-1} , and the Lifting Condensation Level
207 (LCL) was located at 840 hPa. The temperature at LCL, which is generally at the same height
208 as the convective cloud base, was 15°C . The vertical profile of the water vapor mixing ratio
209 also shown in Figure 1b. The water vapor mixing ratio at the surface was around 11.8 g kg^{-1}
210 which decrease rapidly to 2 g kg^{-1} at 5 km.

211



212 **Figure 1.** (a) The *skew T* plot from May 20, 2011, sounding. The air temperature is
213 represented by the solid black line, while the dew point temperature is represented by a
214

215 dashed grey line. The moist adiabat is represented by a dotted red line. The shaded region
 216 between moist adiabat and temperature line represents convective available potential energy
 217 (CAPE). The LCL is also mentioned in the plot. (b) Vertical profile of water vapor mixing
 218 ratio on 20 May 2011 at 00 UTC.

219

220

221 2.2 Aircraft Observations

222 The *in situ* cloud microphysical observations used in this study were obtained from a
 223 University of North Dakota Citation II aircraft. The aircraft collected observations of cloud
 224 microphysical parameters from the cloud base (1.8 km above MSL) to a maximum altitude of
 225 7.5 kilometers above MSL. The MC3E campaign collected extensive airborne measurements
 226 of aerosols and cloud microphysical properties over north-central Oklahoma. A detailed
 227 description of the scientific objectives of the MC3E program, including the field experiment
 228 strategy, airborne and ground-based instrumentation, is given in the paper by Jensen et al.
 229 (2016). This section summarizes the instrumentation used in the current study.

230 **Table 1:** Details of aircraft instruments used in this study.

Instrument	Measurement	Typical range
Cloud imaging probe (CIP) by Droplet Measurement Technologies (DMT)	Size distribution of cloud and precipitation particles	0.025–1.5 mm (0.2–1 mm for model validation in the current study)
2D cloud imaging probe (2D-C) (PMS)	Size distribution of cloud and precipitation particles	0.03–1.0 mm (0.2–1 mm for model validation in the current study)
Cloud droplet probe (CDP) (DMT)	Cloud droplet spectra	2–50 μm
High-volume precipitation	Precipitation particle	0.15–19.2 mm

spectrometer, version 3 (HVPS-3) (SPECinc)	spectra	
King hot-wire liquid water content (LWC) probe (DMT)	Cloud liquid water	0.01–5 g m ⁻³
Temperature probe	Ambient air temperature	–
Static pressure sensor	Ambient air pressure	–

231

232

233 The Citation aircraft was equipped with a standard suite of meteorological instruments, which
 234 provided high-resolution measurements of temperature, pressure, and humidity. In addition, it
 235 carried microphysical probes for cloud and precipitation, and liquid water content, as listed in
 236 Table 1.

237

238 Particle size distributions (PSDs) from cloud to precipitation particle sizes were measured
 239 with various probes, including a 2D Cloud Imaging Probe (2D-C), a Cloud Imaging Probe
 240 (CIP), and a High-Volume Precipitation Spectrometer Probe (HVPS). The 2D-C and CIP
 241 probe data were processed objectively using the algorithm developed at the National Center
 242 for Atmospheric Research (NCAR) to mitigate artifacts produced by shattering on the probes'
 243 leading edges (Field et al. 2006). The 2D-C probe was equipped with anti-shattering tips
 244 (Korolev et al., 2011), while the CIP did not have anti-shattering tips. The size distribution of
 245 cloud drops with diameters from 2 to 50 μm was measured using a Cloud Droplet Probe
 246 (CDP). A King hot-wire liquid water content (LWC) probe measured the LWC. Vertical
 247 velocity is derived from air motion sensing systems available on the research aircraft.

248

249 *2.3 Ground-based measurements*

250 A comprehensive instrumentation suite deployed at the ARM-SGP central facility provided
251 continuous measurements of atmospheric gases, aerosols, clouds, and local meteorological
252 conditions (e.g., wind, temperature, precipitation, and atmospheric profiles). A cloud
253 condensation nuclei (CCN) counter (CCN-100) (DMT) measured the CCN number
254 concentration at seven supersaturation values with a temporal resolution of 1 hour. Surface
255 precipitation was measured with 16 rain gauge pairs placed within a 6-kilometer radius of the
256 SGP CF.

257

258 During the MC3E campaign, the measurement facility deployed at CF measured the spatial
259 variability of surface fluxes of heat, moisture, and momentum. A radiosonde array of 6 sites,
260 covering an area of 300 km × 300 km, was designed to capture the large-scale variability of
261 the atmospheric state. Radiosonde observations (Vaisala RS92-SGP) were conducted with a
262 6-hour frequency (four times daily) at around 05:30, 11:30, 16:30, and 22:30 UTC, providing
263 vertical profiles of atmospheric state variables (pressure, temperature, humidity, and winds)
264 of the environment surrounding the ARM SGP site. When aircraft operations were planned
265 based on forecasted convective conditions, the sounding frequency was increased to a 3-hour
266 frequency with the starting time at 05:30 UTC.

267

268 In addition to airborne observations, the ARM radar network was used to conduct unique
269 radar observations during the MC3E campaign. The information about various radar assets
270 during MC3E is given by Jensen et al. (2016). The surface precipitation used for model
271 validation in this study is a radar-based precipitation estimate as described by Giangrande et
272 al. (2014). They used radar observations from the C-band and X-band scanning ARM
273 precipitation radars (C-band Scanning ARM Precipitation Radar and X-band Scanning ARM

274 Precipitation Radars, respectively) to estimate rainfall within 100 km of the ARM facility in
275 Lamont, Oklahoma. Their radar-based rainfall retrievals were in good agreement with
276 observations with an absolute bias of less than 0.5 mm for accumulations less than 20 mm.

277

278 The Interagency Monitoring of Protected Visual Environments (IMPROVE) network stations
279 close to the location of airborne observations provided ground-level measurements of various
280 chemical species. These included carbonaceous compounds (black and organic carbon), salt,
281 ammonium sulfate, and dust. The details of the measurement techniques used for mass
282 mixing ratios of these compounds are summarized in Malm et al. (1994). The measurements
283 of these aerosol species from various IMPROVE sites, including Ellis (36.08°N, 99.93°W),
284 Stilwell (35.75°N, 94.66°W), and Wichita Mountains (34.73 °N, 98.71°W) sites in Oklahoma,
285 were averaged to provide inputs to AC. Initial mass concentrations for the aerosol species of
286 AC (11 species) including sulfate, sea salt, dust, black carbon, soluble organic, biological and
287 non-biological insoluble organic (five groups of PBAPs) were derived from the Goddard
288 Chemistry Aerosol Radiation and Transport (GOCART) model (Chin et al. 2000). The
289 prescribed mass mixing ratios of aerosol species in A are based on IMPROVE observations
290 and are enlisted in Table 2. It should be noted that for the MC3E case considered in this
291 study, coincident IMPROVE measurements were not available. The mean values of the
292 IMPROVE measurements conducted on May 18 and 21 are used to prescribe the mass of
293 various aerosol species.

294 **Table 2:** The mass mixing ratio of aerosol species based IMPROVE observations which are
295 used as input to AC.

Aerosol species	Mass mixing ratio ($\mu\text{g}/\text{m}^3$)
(NH ₄) ₂ SO ₄	0.56
Dust	0.18
Sea salt	0.021

Black carbon	0.093
Soluble organic carbon (80 % of TOC)	0.45
Insoluble organic carbon (20 % of TOC)	0.18
PBAPs (50% of Insoluble organic carbon)	FNG=0.036; BCT=0.012; PLN=0.028; DTS=0.016; ALG=0.000022

296

297

298

299 **3. Methodology**

300 *3.1 Model description*

301 The ‘*aerosol-cloud model*’ (AC) used in this study is a cloud-resolving model (CRM) with a
302 hybrid spectral bin/two-moment bulk microphysics, interactive radiation, and semi-
303 prognostic aerosol schemes (Phillips et al. 2017a, 2020). The model predicts the mass and
304 number concentrations for five types of hydrometeors: cloud liquid, cloud ice (or “crystals”),
305 rain, graupel/hail, and snow. The mixing ratios of the total number and mass of all particles in
306 each microphysical species are treated as model prognostic variables. AC treats all known
307 microphysical processes such as droplet nucleation, ice initiation through primary and
308 secondary processes, and growth processes such as deposition/sublimation of ice particles,
309 condensation/evaporation of drops, freezing/melting, as well as coagulation by collisions
310 between various hydrometeor types. Both cloud-base and in-cloud activation of aerosols to
311 form cloud-droplets are treated explicitly, with the predicted in-cloud supersaturation
312 resolved on the model grid being used to activate aerosols aloft. Bin-resolved size
313 distributions of each aerosol species are predicted for the interstitial and immersed

314 components of each aerosol species. Extra prognostic variables track the number of aerosols
315 in each aerosol species that have been lost by INP and CCN activation.

316

317 Secondary ice formation is represented by four types of fragmentation:

- 318 • breakup in ice–ice collisions (Phillips et al. 2017a, b) (most active between -10 to -
319 20°C);
- 320 • Hallett and Mossop (1974), rime splintering (most active between -3 to -8°C) ;
- 321 • fragmentation of freezing rain/drizzle by modes 1 and 2 (Phillips et al. 2018) (most
322 active around -15°C);
- 323 • and sublimation breakup (Deshmukh et al. 2021) (most active between -0 to -18°C).

324 The empirical parameterization (EP) (Phillips et al. 2013) of heterogeneous ice nucleation
325 treats all known modes of ice formation (deposition mode, condensation-/immersion-
326 freezing, inside-out and outside-in contact-freezing) in terms of dependencies on the loading,
327 size, and chemistry of multiple aerosol species. In the previous version of the EP, prior to
328 PT21, there were four species of INP aerosol. One of these was PBAP INPs. However, that
329 version of the EP did not resolve the individual types of PBAP INP, which exhibit a wide
330 range of ice-nucleating abilities. The current version of AC also includes the ice nucleation
331 (IN) activity of dust and black carbon. The ice nucleation parameterization of dust, as well as
332 black carbon, is based on studies by Phillips et al. (2008) and (2013). The activation of dust
333 and black carbon INP starts at temperatures colder than -10 and -15°C.

334

335 There are two types of homogeneous freezing represented: that of cloud droplets near -36°C
336 and that of solute aerosols at colder temperatures. Both schemes are described by Phillips et

337 al. (2007, 2009). For cloud droplets, a look-up table from simulations with a spectral bin
338 microphysics parcel model treats the fraction of all supercooled cloud droplets that evaporate
339 without freezing near -36°C , depending on the ascent, initial droplet concentration and
340 supersaturation. The size dependence of the temperature of homogeneous freezing is
341 represented.

342

343 In a recent study, PT21 provided an empirical formulation for multiple groups of PBAP INPs
344 based on field observations over the central Amazon. In this study, we modified AC by
345 implementing the recent empirical parameterization of PBAP INPs by PT21. A summary of
346 their formulation is provided in section 3.2.

347

348 Cloud processes and rainfall formation have been detected using different radar variables,
349 such as specific differential phase K_{DP} . Moisseev et al. (2015), for example, noted an increase
350 in observed K_{DP} because of aggregation. In addition, a few studies have hypothesized
351 evidence of SIP via K_{DP} (e.g., Sinclair et al. 2016; Kumjian and Lombardo 2017; Carlin et al.
352 2021). In this study, we attempted to detect secondary ice formation signatures by
353 implementing K_{DP} estimations into AC. Based on Ryzhkov et al. (2011), K_{DP} values were
354 estimated for various hydrometeor types, including cloud drops, raindrops, cloud ice, snow,
355 and graupel (their equations 22, 23, 24, 26, and 29). The scattering amplitudes were
356 calculated using the Rayleigh approximation. The K_{DP} estimations are made for 0° elevation
357 angle and S-band (radar wavelength of 11 cm). The equivalent volume diameter of the given
358 hydrometeor was used for all calculations.

359

360 *3.2 Empirical formulation for PBAP INPs:*

361 The empirical formulation by PT21 for multiple groups of PBAPs includes: - 1) fungal spores
 362 (FNG), 2) bacteria (BCT), 3) pollen (PLN), 4) viral particles, plant/animal detritus (DTS), 5)
 363 algae (ALG) and their respective fragments are implemented in AC. This formulation is
 364 based primarily on field observations over the central Amazon rainforest, with empirically
 365 derived dependencies on the surface area of each group (except algae) and it applies to the
 366 particles with diameters greater than 0.1 μm . Here, we summarize the formulation by PT21
 367 briefly.

368 For $X = \text{FNG, PLN, BCT, and DTS}$

$$369 \quad n_{IN_BIO,X} = \int_{\log[0.1 \mu\text{m}]}^{\infty} \{1 - \exp[-\mu_X]\} \times \frac{dn_X}{d\log D_X} d\log D_X, \quad (1)$$

$$370 \quad \mu_X = H_X(S_i, T) \xi(T) \times \text{MIN}\{[\exp(-\gamma_X T) - 1], 40\} \times \frac{1}{\omega_{X,1*}} \frac{d\Omega_X}{dn_X} \quad \text{for } T < 0^\circ \text{C} \quad (2)$$

371 In equation (1), $n_{IN_BIO,X}$ is the number mixing ratio of INP active at temperature T for given
 372 species X ; Ω_X is the total surface area mixing ratio of particles with diameters D_X greater than
 373 0.1 μm ; $d\Omega_X/dn_X \approx \pi D_X^2$. The normalized size distribution of given bioaerosol species is
 374 given by $dn_X/d\log D_X$. In Eq (2), H_X is the empirically determined fraction that inhibits
 375 nucleation in substantially water-subsaturated conditions. The factor ξ varies between 0 to 1
 376 and considers the fact during laboratory experiments drop freezing was not observed at
 377 temperatures warmer than a certain threshold in the laboratory observations. The parameter
 378 $\omega_{X,1*}$ depends on bioaerosol type with the dimensions of area (m^2). The values of
 379 $\omega_{X,1*}$ shown for PLN and DTS are 0.1 m^2 . For FNG and BCT the values of $\omega_{X,1*}$ are
 380 9.817×10^{-5} and $9.12 \times 10^{-5} \text{ m}^2$ respectively. The slope of the fitted curve (γ_X) has a
 381 constant value of 0.5 C^{-1} .

382

383 The concentration of algal particles at the ATTO site was much smaller than our detection
 384 threshold, so we could not use a similar empirical treatment for ALG. The frozen fraction for
 385 the algal particles (Diatom cell, *Thalassiosira pseudonana*) available in the literature is used
 386 to estimate INPs from ALG (Wilson et al. 2015). The frozen fraction is given by eq. (3)

$$387 \quad f_{alga e}(T) = A_1 + \frac{(A_2 - A_1)}{1 + 10^{(B+T) \times p}} \quad (3)$$

388 where $A_1 = -0.03$, $A_2 = 0.993$, $B = 27.73$, and $p = 0.399$.

389 Also $f_{alga e}(T) = 0$ at $T > -24^\circ C$ and $f_{alga e}(T) = 1$ at $T < -35^\circ C$

390 For the given concentration of algal particles in the air ($n_{alga e}$) the active INP from ALG is
 391 given by

$$392 \quad n_{IN_BIO,X} = f_{alga e} \times n_{alga e} \quad (4)$$

393

394

395 3.3 Model setup

396 AC was driven by initial and evolving boundary data for meteorological conditions. The
 397 large-scale advection of humidity and temperature tendencies maintained the convection.
 398 Convection was initiated by imposing perturbations onto the initial field of vapour mixing
 399 ratio. The large-scale forcing condition used for the simulation was derived using the
 400 constrained variational analysis method described in Xie et al (2014). Based on this method,
 401 the so-called large-scale forcing including large-scale vertical velocity and advective
 402 tendencies of temperature and moisture were derived from the sounding measurements
 403 network. During the MC3E campaign, the sounding network consists of five sounding
 404 stations centered on a sixth site at the ARM SGP central facility (CF). An area with a

405 diameter of approximately 300 km was covered by this sounding network covers. Additional
406 details about the sounding data are described in section 2.3. Figure S1 shows the time height
407 evolution of potential temperature and water vapor mixing ratio from large-scale forcing data.
408 It also shows the time variation of CAPE based on observations. The maximum value of
409 CAPE 2400 JKg^{-1} was noticed around 12 UTC on 20th May.

410

411 The model simulations were carried out for a three-dimension domain of 80 km x 80 km with
412 horizontal grid spacings of 2 km. In vertical, the model resolution was 0.5 km, and the model
413 top was located at about 16 km. The lateral boundary conditions are doubly periodic on all
414 sides of the domain. The initial time of the simulations was at 1200 UTC on 19 May 2011
415 and all simulations were performed for 48 hours at a time step of 10 seconds.

416

417 The GOCART model (Chin et al. 2000) was used to initialize the seven chemical species
418 associated with the EP. The data from the three IMPROVE sites mentioned above (Section
419 2.3) was used to rescale the mass concentration profiles at all levels so that they match the
420 measurements near the surface. Table 2 lists the mass mixing ratios of various aerosol species
421 after the corrections. The corresponding vertical profiles of various aerosol species including
422 sulfate, dust, sea salt, black carbon, and total organic carbon are shown in Supplementary
423 Figure S2 (panel a-e). The corresponding IMPROVE measurements are also shown in the
424 same Figure. There were no direct measurements of PBAP mass during IMPROVE and
425 therefore it was derived from the measured mass of the total organic carbon (TOC). The
426 relative contribution of insoluble and soluble organic carbon to TOC was assumed to be 20%
427 and 80%, respectively by assuming a water-soluble fraction of 80% for carbonaceous aerosol
428 (Phillips et al. 2017b). AC takes into account the soluble fraction of each type of aerosol. The

429 values of this factor are 0.15 for dust, and 0.8 for carbonaceous species. The value of this
430 fraction for all PBAP groups is 0.1.

431

432 There are very observations available in the literature showing the fraction of PBAP in the
433 insoluble organics or total aerosol particles. For example, observations by Matthias-Maser et
434 al. (2000) found that 25% of the total insoluble particles are biological. PBAPs can contribute
435 a significant fraction to the number concentrations of total aerosol particles (Mattias-Maser et
436 al., 1999). Mattias-Maser and Jaenicke (1995) showed that PBAPs can amount to 20% and
437 30% of the total aerosol particles. The observation by Jaenicke (2005) in a semi-rural location
438 showed that cellular particles can contribute up to about 50% of total particles. Based on
439 these studies we assumed that 50% of the insoluble organics were biological in origin. The
440 total PBAP loading was prescribed partly based on observations of insoluble organics. The
441 mass fraction of each PBAP group in total PBAP mass is prescribed based on the PT21
442 observations. The fraction of mass mixing ratio for various PBAP groups is: FNG= 0.39,
443 BCT= 0.13; PLN= 0.31; DTS= 0.17; ALG= 2.5×10^{-4} .

444

445 It should be noted that the observations of PBAPs over different geographical locations
446 (including the region where we carried out the simulation) are rare, which prevents us from
447 using the region-specific PBAP observations for the present study. Hence, PT21's default
448 observations were used to calculate the relative contribution of various PBAP groups to
449 insoluble organics. The parameters for the shape of PSD of each PBAP group (modal mean
450 diameters, standard deviation ratios, and relative numbers in various modes) are prescribed
451 based on observations from Amazon (PT21). Supplementary Figure S3 depicts the
452 corresponding size distribution of various PBAP groups in AC. The figure depicts unimodal

453 size distribution for FNG, BCT, PLN, and ALG, whereas DTS has a bimodal size
454 distribution. To check the validity of the observation from PT21 over the region considered in
455 the current study, the model estimated values of one of the major PBAP bacteria are
456 compared with the observations as shown in Figure S4. It shows that the estimated values of
457 bacterial number concentration are overall in fair agreement with previous observations (e.g.
458 Bowers et al 2009; Bauer et al. 2002; Burrows et al. 2009). The simulated bacterial ($\sim 10^4 \text{ m}^{-3}$)
459 and fungal ($\sim 10^3 \text{ m}^{-3}$) number concentration by AC is in good agreement with their typical
460 concentration in the atmosphere (Després et al. 2012). The resulted vertical profiles of mass
461 of the various PBAP groups are shown in Figure S2 (panel f).

462

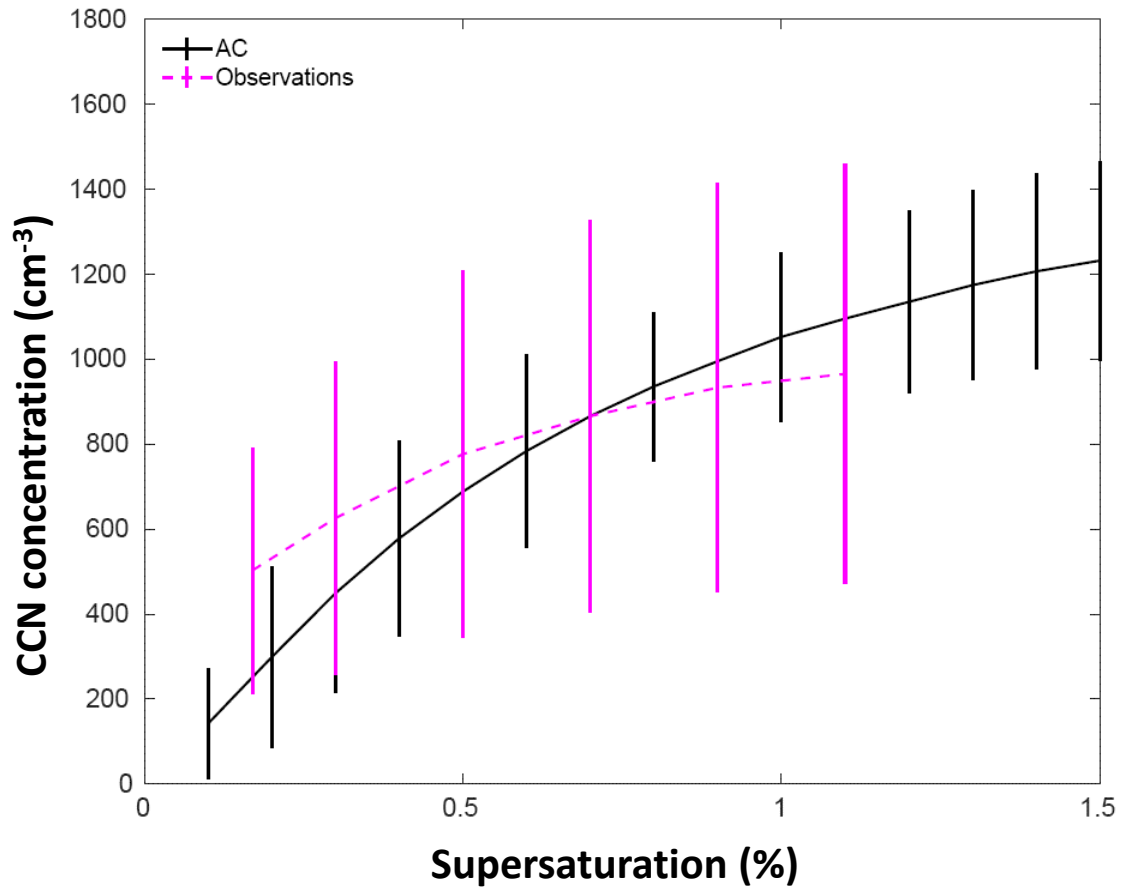
463 From these prescribed loadings of aerosol species, AC predicts their size distribution and
464 hence the CCN activity spectrum. Using the initial sounding and aerosol profile, AC can
465 predict the in-cloud size distribution of aerosols in each species as well as in-cloud
466 supersaturation. To validate this prediction, Figure 2 shows the predicted CCN spectrum
467 compared with observations from the CCN counter at the surface at the SGP site.

468

469 It should be noted that the aerosol mass loading from IMPROVE observations showed
470 variations of 20-30% for the simulated case. The uncertainties in the input aerosol mass
471 loading can result in simulated CCN concentration and are shown by the errors in the CCN
472 concentration predicted by the AC. During 19-20 May, the measured number concentration
473 of active CCN at the SGP CF ranged from 400 to 3000 cm^{-3} at 1% supersaturation (Fridlind
474 et al. 2017). The measurements were made on 20 May before the start of the rain in clear air.

475

476



477

478 **Figure 2.** The CCN spectrum from AC for a simulated squall line case on May 20, 2011, for
479 an environment 500 meters above MSL. The predicted CCN spectrum is compared to the
480 observed CCN spectrum at the SGP CF (300 m above MSL). The error bars on the model
481 predicted CCN concentration are associated with uncertainties in the input values of mass
482 mixing ratios of various aerosol species that act as CCN.

483

484 The normalized CCN number concentrations at 1% supersaturation from observations and
485 AC are $\sim 1000 \text{ cm}^{-3}$ and $\sim 940 \text{ cm}^{-3}$, respectively. Given the wide range of observed CCN
486 concentrations at each supersaturation as well as the uncertainties in the model predicted
487 CCN concentration, the predicted and observed CCN activity spectra are in acceptable
488 agreement.

489

490

491 **4. Results from control simulation and model validation**

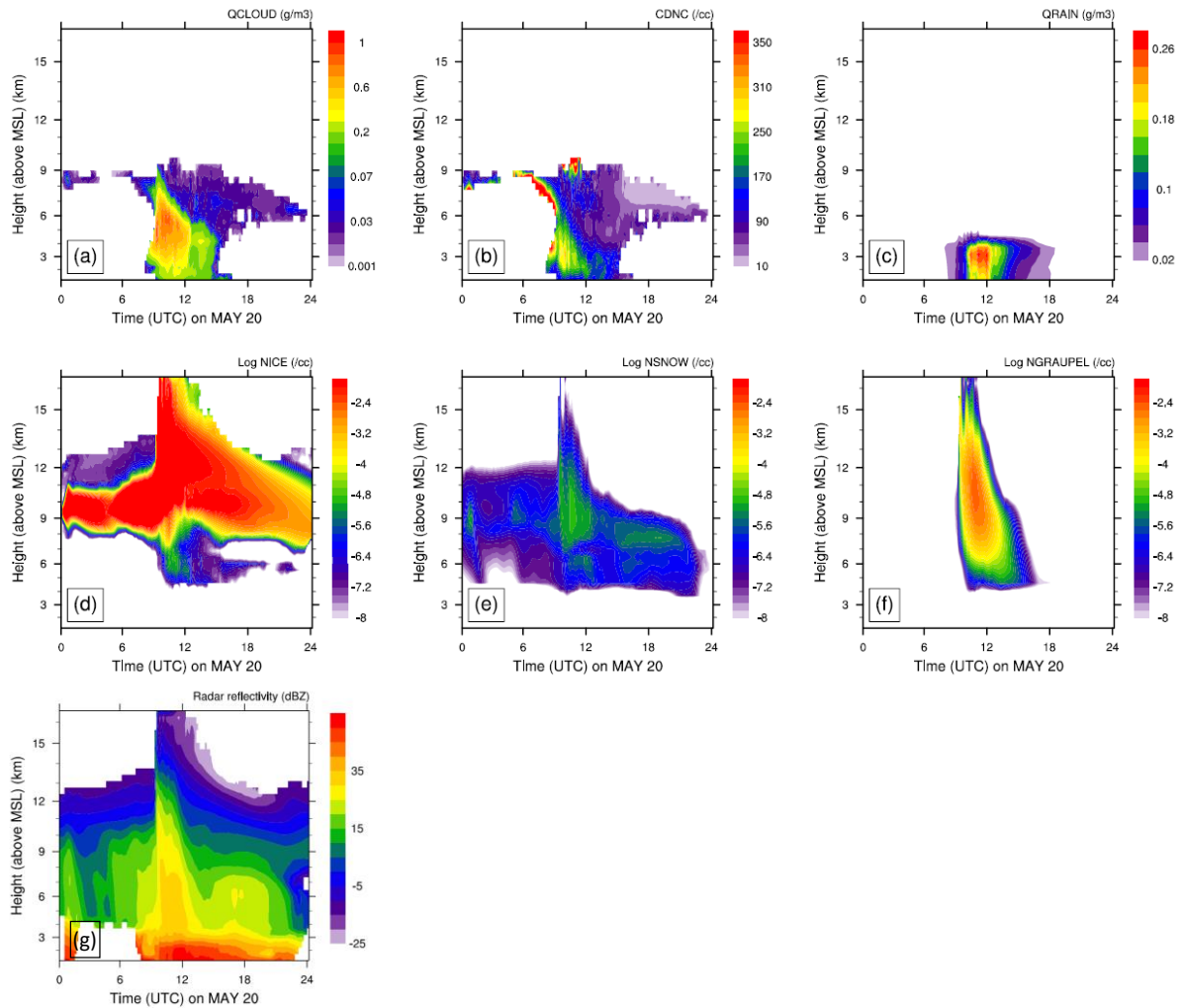
492 *4.1 Overview of the control simulation*

493 An intense north-to-south oriented squall line moved over the ARM SGP CF on May 20,
494 2011, from 1100 to 1400 UTC (Sec. 2.1). The new version of AC simulated this case, after
495 implementing the empirical formulation by PT21 for multiple groups of PBAP INPs
496 ('control' simulation) (Sec. 3). It should be noted that five ensemble runs were carried out for
497 control simulation (See Table 3) varying the perturbing in the initial water vapor mixing
498 ratio.

499

500 Figure 3 shows the time-height evolution of various liquid and ice cloud microphysical
501 parameters derived from the control simulation conditionally averaged over cloudy regions.
502 The maximum average cloud droplet number concentration was around 250 cm^{-3} . The LWC
503 was typically less than 0.5 g m^{-3} . The freezing level (0°C) was around 4.1 km above MSL.
504 The deep convection began around 10 UTC, followed by intense precipitation around 11
505 UTC, and reached its peak around 12 UTC. The time-height evolution of cloud ice, snow,
506 and graupel number concentrations shows maxima shortly before 12 UTC, which coincides
507 with the time of peak precipitation. This suggests that the ice phase was important in
508 precipitation formation.

509



510

511 **Figure 3:** Time-height contours of domain averaged a) cloud water mixing ratio (QCLOUD);
 512 b) cloud droplet number concentration (CDNC); c) rainwater mixing ratio (QRAIN); d)
 513 number concentration of cloud ice (NICE); e) number concentration of snow (NSNOW); f)
 514 number concentration of graupel (NGRAUPEL). Due to a wide range of values, the log
 515 values number concentrations are plotted. The surface height is ~ 500 m. The averaging was
 516 done for cloud points with $LWC > 0.001\text{gm}^{-3}$ or total water content (TWC) $> 10^{-6}\text{gm}^{-3}$. Also
 517 shown is the time-height evolution of domain averaged (g) radar reflectivity.

518

519 The time-height map of simulated radar reflectivity during 20 May, unconditionally averaged
 520 over the whole domain is shown in Figure 3g. It shows the well-defined squall line passing
 521 over the domain from 1100 to 1500 UTC. The maximum of this domain-wide simulated
 522 reflectivity is around 40 dBZ (Fig. 3d) when deep convection was happening. The
 523 instantaneous maximum of reflectivity at any grid-point (not shown) was about 50 dBZ. At

524 other times, the average reflectivity was typical of the stratiform cloud of about 15 dBZ. The
525 cloud top height of the squall line decreases after 1400 UTC.

526

527

528 *4.2. Model validation against coincident observations of the storm*

529 The extended stratiform region of the squall line while in the vicinity of the SGP CF was
530 sampled by the Citation aircraft equipped with a full suite of cloud microphysical
531 instrumentation (Sec. 2). The aircraft started sampling the stratiform precipitation region at
532 around 1300 UTC and continued the observations at sub-freezing temperatures from 1335 to
533 1515 UTC. Occasionally, the aircraft encountered weak convective updrafts (< 6 m/s). The
534 aircraft actively avoided convection that was more vigorous than that. In this section, we
535 validate various microphysical and dynamical quantities from the control simulation against
536 aircraft and ground measurements. The control run includes all primary and SIP processes of
537 ice initiation. The vertical profiles shown here are an average of five ensemble runs.

538

539 Figure 4 compares the aircraft observations against predicted microphysical quantities, with
540 both the predictions and observations identically averaged, conditionally over convective ($6 >$
541 $|w| > 1$ m/s) and stratiform regions ($|w| < 1$ m/s). The simulated LWC decreases exponentially
542 with height above the cloud base. There is considerable scatter in observed LWC at each
543 level. The various degrees of dilution of sampled parts of the cloud can cause these
544 variations in LWC at a given altitude. The maximum simulated LWC of 0.5 gm^{-3} was
545 observed in the convective region at temperatures warmer than -5°C . In the convective region
546 around -5°C , the measured LWC is lower than the simulated LWC by a factor of 3. For the

547 stratiform region, simulated values of LWC are in adequate agreement with observations.
548 Overall, the means of observed LWC are in acceptable agreement with the model results for
549 convective as well as stratiform regions.

550

551 The vertical profiles of simulated and observed Cloud Drop Number Concentration (CDNC)
552 (Fig. 4c and 4d) showed that CDNC was lower than 300 cm^{-3} . In the convective region, the
553 measured CDNC is 40% lower than the simulated CDNC at 15°C . However, an adequate
554 agreement between them is found around -5°C . For the stratiform region, simulated CDNC is
555 much higher in the mixed-phase region. However, at a temperature warmer than 0°C the
556 values of observed CDNC are in acceptable agreement with observations. The observed and
557 simulated mean diameter of cloud droplets varied between 6 to $15 \mu\text{m}$ over height (Figures 4e
558 and 4f). There are few points in the convective region e.g., around -5°C , where the observed
559 cloud drop diameter is 50% lower than the simulated value. An adequate agreement between
560 simulated and observed cloud drop diameter was found for the stratiform region. Overall, the
561 predictions of average CDNC and cloud droplet diameter, in both convective and stratiform
562 regions, show a fair agreement with observations.

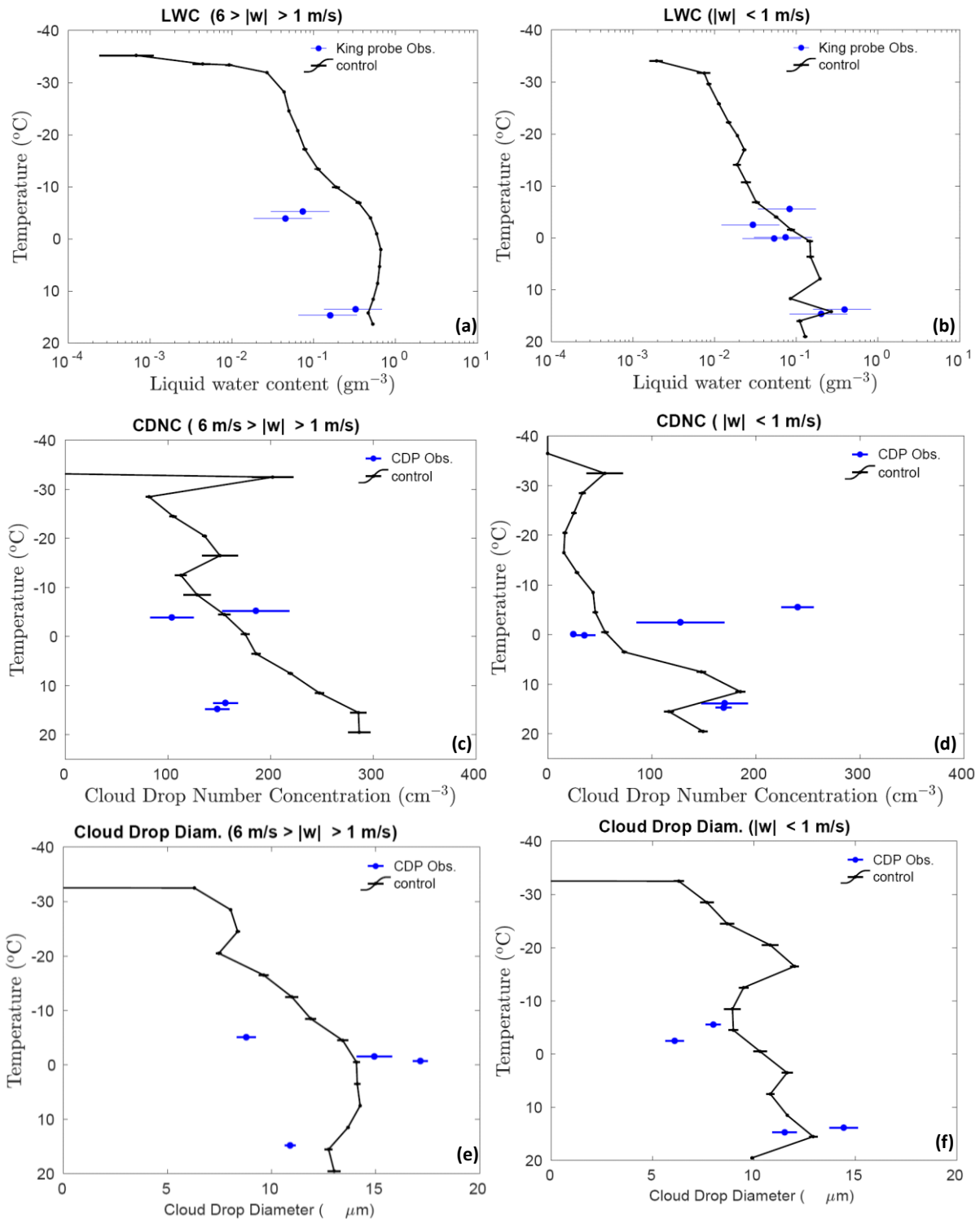
563

564 The ice particle number concentration from observations and the control simulation is also
565 compared as shown in Figures 5a and 5b for convective and stratiform regions, respectively.
566 It should be noted that the observed number concentration of ice particle particles smaller
567 than $200 \mu\text{m}$ is prone to shattering, even with the use of the shattering correction algorithm.
568 This can introduce a significant bias in the observed ice number concentration (Korolev et al.,
569 1991). To avoid these biases, we have compared the number concentration of ice particles
570 with a diameter greater than $200 \mu\text{m}$ from both observation and model (denoted by 'NT200').

571 However, in the rest of the manuscript (in sensitivity studies), the number concentration from
572 the model included ice particles of all size ranges.

573

574



575

576 **Figure 4:** Comparison of the control simulations by AC with aircraft observations, for liquid
577 water content conditionally averaged over (a) convective ($6 \text{ m/s} > |w| > 1 \text{ m/s}$) and (b)
578 stratiform ($|w| < 1 \text{ m/s}$) regions; cloud drop number concentration over (c) convective and (d)
579 stratiform regions; average size of cloud droplets ($< 20 \mu\text{m}$) conditionally averaged over (e)
580 convective and (f) stratiform regions. All the vertical profiles shown here are averaged for the
581 whole domain. The error bars were estimated based on five ensemble runs.

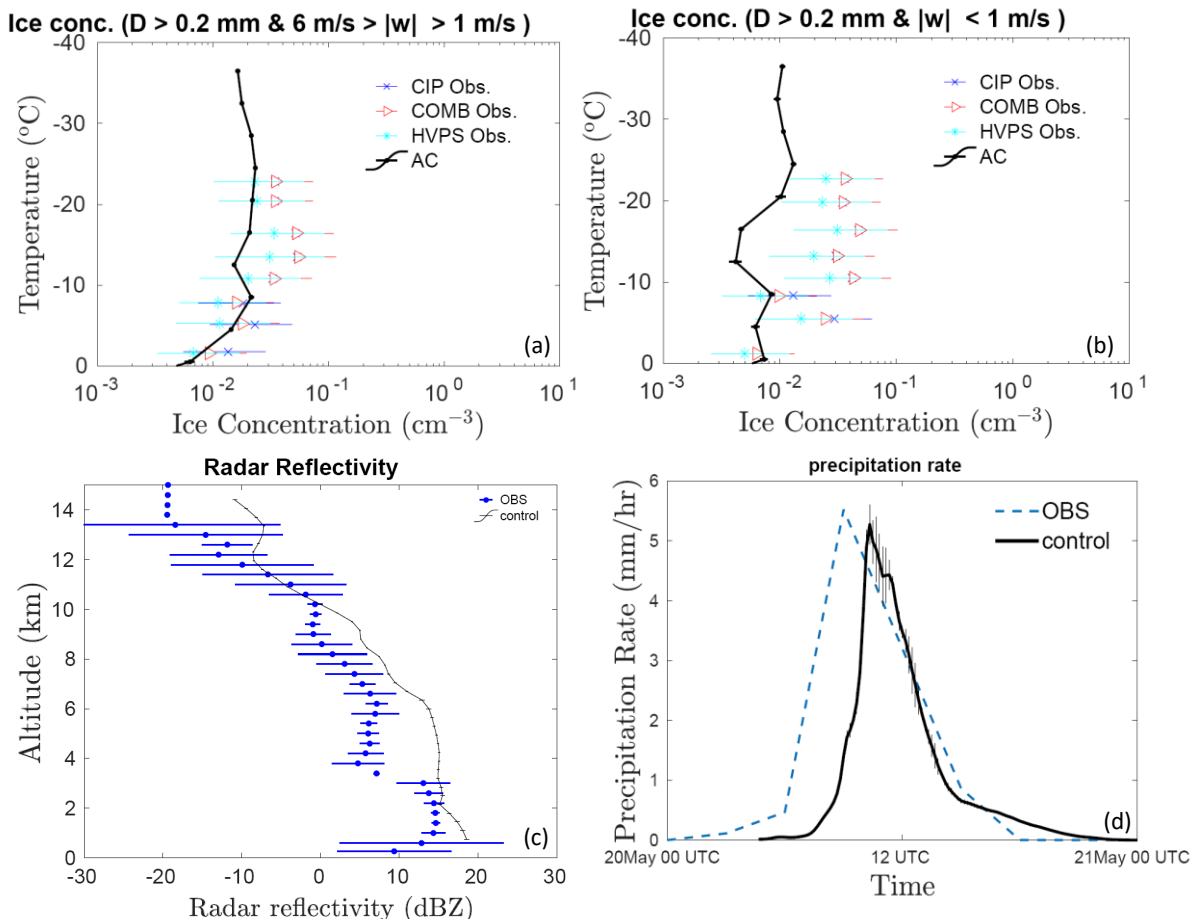
582

583 Observations show that the concentration of ice particles gradually increases as the
584 temperature decreases, as expected. The maximum ice number concentration from the aircraft
585 observations (with $D > 200 \mu\text{m}$) is $\sim 0.06 \text{ cm}^{-3}$ around $-15 \text{ }^\circ\text{C}$. Good agreement to within 50%
586 at most levels, was found between the model simulated NT200 and that observed for the
587 convective region.

588

589 In the stratiform region, at most levels, model values of NT200 have the same order of
590 magnitude as observations. However, between about the -10 and -16°C levels, the stratiform
591 NT200 values are about half an order of magnitude lower than the observations. In similar
592 simulations of the 20 May case, Fan et al. (2015) and Fridlind et al. (2017) also showed
593 underestimation of simulated ice number concentrations. Compared to observations, their
594 simulations showed half an order of magnitude bias in ice crystal number concentration.
595 Comparatively, for the convective region, our model predicted ice number concentrations
596 were in better agreement with observations. As mentioned in section 2.2, imaging probe data
597 is prone to shattering, and various corrections were used to rectify it. However, there are
598 currently no ways to determine how many undetected artifacts remain after shattering
599 corrections have been applied (Baumgardner et al. 2022). Such uncertainties in measured ice
600 number concentration could result in such bias in observed and simulated ice number
601 concentrations. In summary, though the AC model is not totally perfect, it did a fair job in
602 simulating observed ice number concentrations.

603



604

605

606 **Figure 5:** Comparison of the control simulations by AC with aircraft observations, for ice
607 number concentration of all particles > 0.2 (NT200) mm in the maximum dimension of all
608 microphysical species (cloud ice, graupel/hail, snow), averaged over (a) convective (6 m/s $>$
609 $|w| > 1$ m/s) and (b) stratiform ($|w| < 1$ m/s) regions. (c) The vertical profile of simulated
610 radar reflectivity conditionally averaged over all regions of significant reflectivity (> -20
611 dBZ) at each level is compared with observations from ground-based radars. The temperature
612 corresponding to each altitude is mentioned on the right axes; (d) predicted precipitation rate
613 (mm/hr) compared with ground observations at the SGP CF. All the vertical profiles shown
614 here are averaged for the whole domain. The error bars were estimated based on five
615 ensemble runs.

616

617

618 In Figure 5c, the radar reflectivity from vertically pointing Ka-band ARM zenith radar is
619 compared with the mean profile from model simulations. This figure illustrates that simulated
620 reflectivity profiles below roughly 3 km and above 8 km MSL altitudes are in good

621 agreement with observations. Between 3 and 8 km MSL (temperatures of 2 and -30°C), the
622 bias in reflectivity from model simulations and observations is about 10 dBZ. Thus, the
623 simulated reflectivity is substantially higher than observed, particularly at levels where the
624 aircraft sampled the clouds. Fridlind et al. (2017), as well as Fan et al. (2015), noticed similar
625 overestimations of reflectivity within stratiform outflow of the squall line case on 20 May.
626 They attributed the reflectivity biases to significantly larger ice particles in the simulations
627 than observed.

628

629 Figure 5d compares the time series of precipitation rate from the control simulation with the
630 radar-based precipitation estimates. In both, control simulation and observations, a maximum
631 precipitation rate of about 5 mm/hr was noticed, with an error in the prediction of less than
632 5%. In comparison to observations, the simulated squall line arrives 1-2 hours later. The lack
633 of resolution of the 3D turbulence in the planetary Boundary Layer and uncertainties
634 associated with the 3D structure of initial and boundary conditions can all have an
635 independent impact on the simulated rainfall structure, resulting in a delayed peak.
636 Nonetheless, AC has done a fair job in simulating the peak in the predicted precipitation rate.

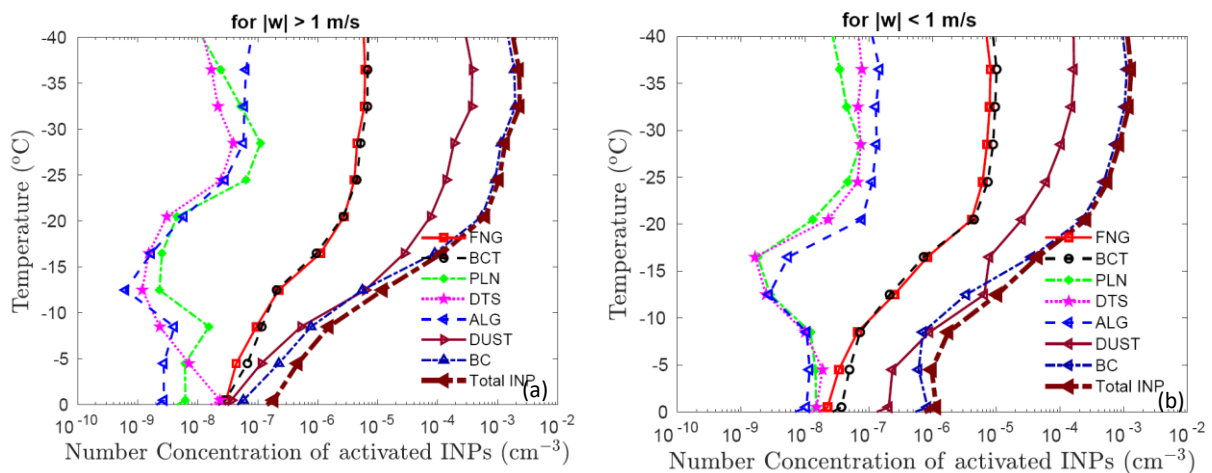
637

638 *4.3 Analysis of simulation with ice particle budgets and tagging tracers*

639 The activated PBAP INPs from the control run are shown in Figure 6 for the convective and
640 stratiform regions. In addition to the PBAP INPs, Figure 6 also shows the activated INPs
641 from dust and black carbon. It should be noted that these concentrations shown here are based
642 on advective tagging tracers that follow the diffusion, ascent, and descent inside cloud
643 motions. Overall, bacterial, and fungal particles dominate the biological INP concentration in

644 the simulated cloud. For example, at -20°C the activated INPs from bacteria and fungi are
 645 higher than the other three groups of PBAP INPs (detritus, pollen, algal) by two orders of
 646 magnitude in both convective as well as stratiform regions. At that level in convective
 647 regions, the average concentration of simulated active PBAP INPs is about $3 \times 10^{-6} \text{ cm}^{-3}$,
 648 which is two orders of magnitude less than the maximum total for all active INPs (about
 649 $3 \times 10^{-4} \text{ cm}^{-3}$) in the whole simulation. Overall, the predicted total INP concentration is
 650 dominated by black carbon and dust. At -10°C , the Activated INPs from dust and black
 651 carbon differ by an order of magnitude from the total PBAP INPs in convection.

652



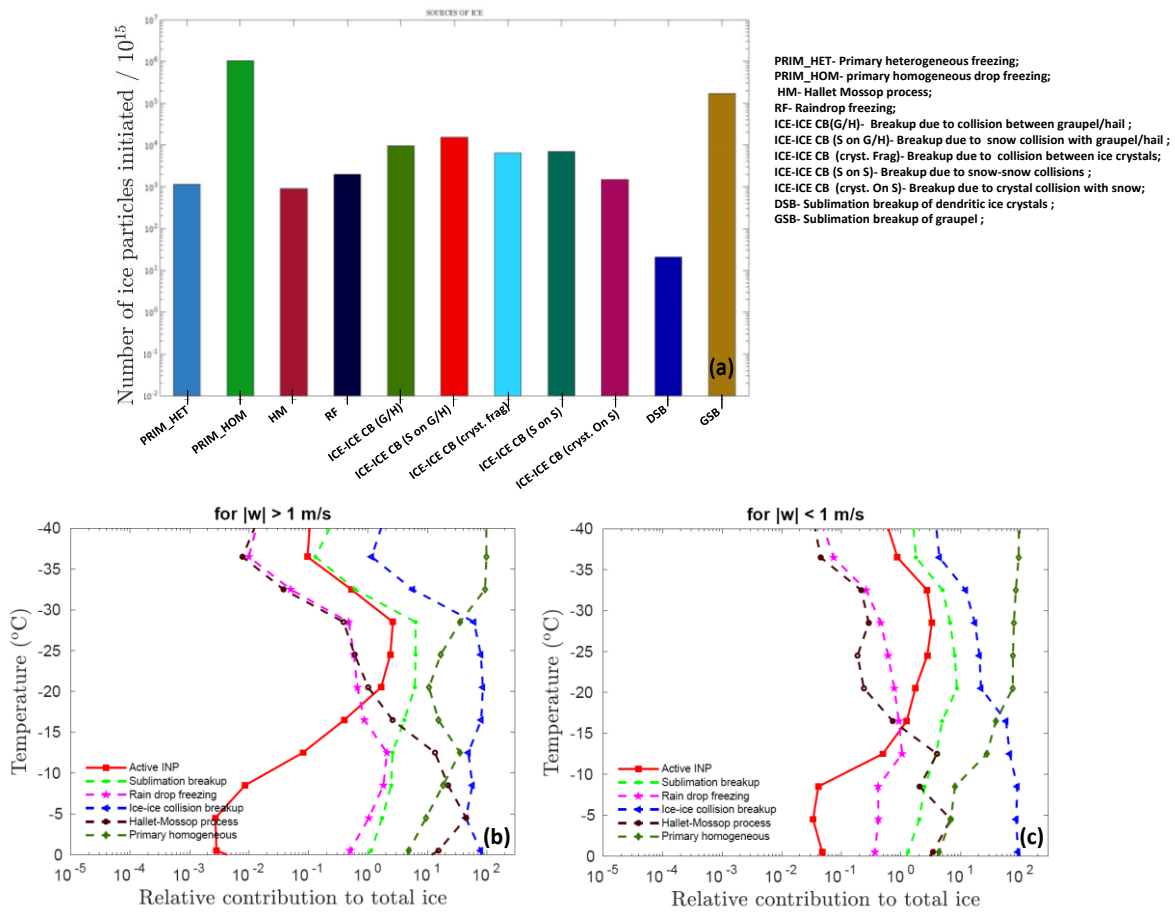
653

654 **Figure 6:** The activated number concentration INPs from various PBAP groups along with
 655 dust (DUST) and black carbon (BC) and total INPs at various temperatures for (a) convective
 656 and (b) stratiform regions. All the vertical profiles shown here are averaged for the whole
 657 domain.

658

659

660 The formation of ice in a cloud is a result of several primary and secondary processes. It is
 661 important to understand the relative importance of these processes in precipitation formation.
 662 To that end, Figure 7a shows the ice particles initiated from various sources throughout the
 663 3D domain of the entire simulation.



665

666

667 **Figure 7:** (a) Ice crystal budget for simulated MC3E case. The number of ice crystals
 668 produced by various mechanisms (as shown in the legend box) per 10^{15} particles is shown. .
 669 Also shown is the relative contribution of various SIP mechanisms such as sublimation
 670 breakup, raindrop freezing, ice-ice collision breakup, and the Hallett-Mossop process to the
 671 total ice number concentration as a function of temperature, averaged conditionally over only
 672 (b) convective and (c) stratiform regions. The relative contribution was calculated based on
 673 advective tagging tracers for the given process. The convective and stratiform regions were
 674 identified based on criteria $|w| > 1$ and $|w| < 1$, respectively.

675

676

677 The primary homogeneous (PRIM_HOM) dominates the total ice budget. Among all SIP
 678 mechanisms, breakup caused by collisions between various ice particles is the most important
 679 in determining total ice number concentration. The ice production by sublimation breakup of

680 graupel is slightly lower than PRIM_HOM. However, the contribution of ice production via
681 sublimation breakup of dendritic ice crystals is negligible.

682

683 Figure 7b and 7c depict the relative importance of ice concentration from various SIP
684 mechanisms, as well as active INPs in determining total ice number as a function of
685 temperature for convective and stratiform regions. Each source of ice displayed is tracked
686 with advective “tagging tracers” throughout the simulation. Overall, at temperatures warmer
687 than -15°C , the contribution to the total ice number concentration from various SIP is 2-3
688 orders of magnitude higher than the concentration of active INPs, highlighting the importance
689 of SIP mechanisms in ice formation. At -25°C , breakup in ice-ice collisions contributes
690 around 75% and 20% of the total ice concentration in the convective and stratiform regions,
691 respectively. At the same temperature, in both convective and stratiform regions, sublimation
692 breakup and raindrop freezing contribute about 8% and 0.8 %, respectively. It can be
693 observed that in the convective regions at temperatures warmer than -30°C , SIP mechanisms
694 are important in determining the total ice concentrations, whereas at colder temperatures
695 homogeneous nucleation is dominant. In the stratiform region, this crossover occurs at a
696 much warmer temperature around -18°C . At temperatures colder than this homogeneous
697 nucleation is a major contributor to the total ice whereas at warmer temperatures SIP
698 mechanisms prevail. Overall, the contribution of active INP to the total ice is lower than 3%.

699

700 Secondary ice formation via the HM process of rime-splintering contributes significantly to
701 ice production at temperatures warmer than about -15°C (Fig. 7b and 7c), enhancing the ice
702 concentration beyond the primary ice. In the convective region, the contribution of the HM
703 process in total ice can reach as high as 40% around -5°C . The simulated cloud droplet

704 diameter is mostly smaller than 15 μm . It is smaller than the cloud droplet size required for
 705 the HM process to occur. In AC, the rate of the rime-splintering mechanism depends on the
 706 concentration of droplets $> 24 \mu\text{m}$. It should be noted that in the AC model HM process is
 707 treated with a factor multiplying the fragment emission which depends on the cloud droplet
 708 size. This factor is zero for cloud diameter below 16 μm and unity above 24 μm with linearly
 709 interpolated in between.

710

711 **5. Results from sensitivity tests about the influence of PBAP**

712 To quantify the effect of multiple types of PBAPs on cloud properties, sensitivity tests were
 713 performed by modifying the control simulation and comparing the perturbed simulations with
 714 it.

715 **Table 3:** Description of various sensitivity simulations carried out in the current study. The
 716 corresponding figures for each simulation are also mentioned.

717

Simulation	PBAP included	Changes in initial PBAP mass	Cloud processes switched on/off	Corresponding figures
control (five ensembles)	ALL PBAPs act as CCN and INP	-	All cloud processes in the AC are on	Figures 4 onward all
no-PBAP (five ensembles)	No PBAP can act as CCN and INP	All PBAPs mass was set to zero	Same as control	Figures 8, 9, 10, 11, 12
no-PBAP INP (five ensembles)	No PBAP can act as INP (CCN activity of PBAP is on)	-	Same as control	Figures 8, 9, 10, 11, 12
high-PBAP (five ensembles)	Same as control	All PBAPs mass was	Same as control	Figures 8, 9, 10, 11, 12

		boosted by a factor of 10		
very high-PBAP (five ensembles)	Same as control	All PBAP mass boosted by a factor of 100	Same as control	Figures 8, 9, 10, 11, 12
ultra high-PBAP (five ensembles)	Same as control	All PBAP mass boosted by a factor of 1000	Same as control	Figure 8, 9
no-sublimation breakup	Same as control	-	SIP from sublimation breakup is off	Figure 13
No-collisional ice-ice breakup	Same as control	-	SIP from the collision between ice particles is off	Figure 13
No-secondary	Same as control		ALL SIP mechanisms are off	Figures 13, 14
very high-PBAP with no secondary	Same as control	All PBAP mass boosted by a factor of 100	ALL SIP mechanisms are off	Figure 14

718

719 Simulations were performed by eliminating all PBAPs from the control (*'no-PBAP'* case) and
720 by multiplying their initial loadings at all levels by factors of 10 and 100 (*'high-PBAP'* and
721 *'very high-PBAP'* cases) respectively. Comparison with the control simulation reveals the
722 overall effect from both the CCN and IN activities of all bioaerosols combined. These factors
723 are justified by considering the variations in PBAP concentrations in the range of about 0.1 to
724 30 L⁻¹ over North American forests (Huffman et al. 2013). An additional simulation was
725 conducted with a 1000-fold increase in initial PBAP loading (*'ultra high-PBAP'*) to
726 investigate if these unrealistically high concentrations of PBAPs could affect the ice phase in
727 a purely hypothetical scenario. Five ensemble runs were carried out for all major simulations

728 involving perturbations in PBAP loading. The ensemble runs were carried out by varying the
729 perturbation in initial conditions (water vapor mixing ratio).

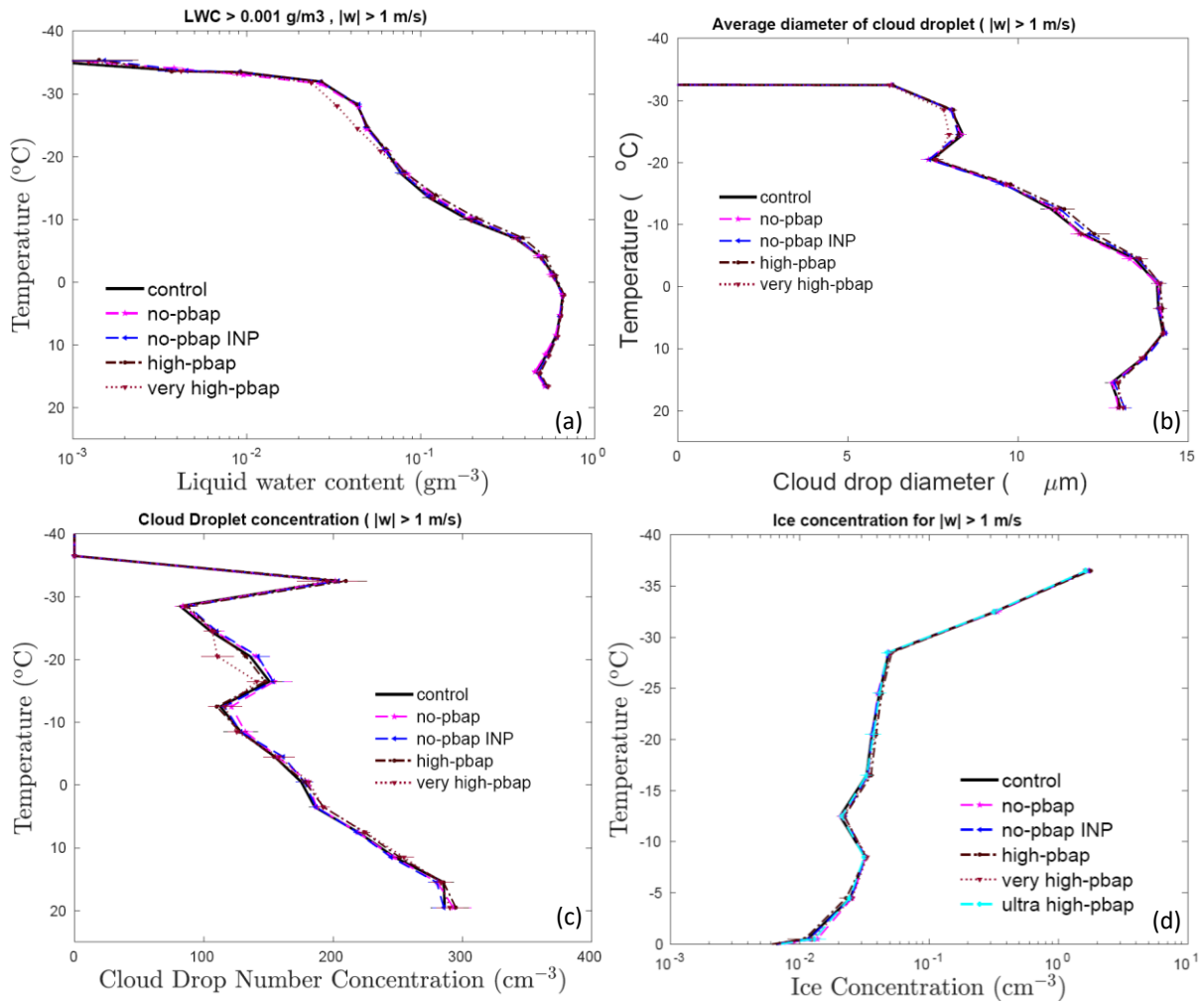
730

731 Additional simulations were performed by removing treatment of biological IN activity in the
732 EP (*'no-PBAP INP'* case) relative to the control run. A comparison of both additional
733 simulations against the corresponding simulations with the full change in the PBAP loadings
734 (no-PBAP and high-PBAP cases) reveals the separate roles of the INP and CCN activities for
735 the changes in biological material. Apart from these changes in PBAPs, the perturbed
736 simulations are identical to the control run.

737

738 Figure 8 reveals the effects of all bioaerosols on cloud properties in the convective region
739 ($|w| > 1$ m/s). Overall, changes in cloud microphysical properties including liquid water
740 content, cloud droplet size, cloud drop number concentration, ice number concentration are
741 less sensitive to the changes in PBAPs for the convective part of the simulated clouds and are
742 not statistically significant. The LWC, cloud droplet number and cloud drop diameter in the
743 perturbed simulations does not differ much ($< 3\%$) from the control run. For the whole storm,
744 considerable changes in the spatial distribution of total ice number concentration are observed
745 due to changes in PBAPs (see Figure S5). However, vertical profiles showed very small
746 changes in the ice number concentrations. In the convective region, changes in ice crystal
747 number concentration due to changes in PBAPs are negligible ($< 6\%$). This includes the
748 extreme changes in bioaerosol loading (ultra high-PBAP case).

749



750

751 **Figure 8:** The temperature dependence of the (a) liquid water content, the (b) cloud droplet
752 number, (c) the cloud droplet diameter, and the (d) total ice number concentration for
753 ‘control’ simulation and various sensitivity runs involving a change in total PBAP number
754 concentrations for in the convective region. The averaging conditions are mentioned at the
755 top of each figure. The ice number concentration from the ultra high-PBAP is also shown in
756 panel d. All the vertical profiles shown here are averaged for the whole domain.

757

758

759

760 **Table 4:** Changes in mean cloud macro and microphysical properties associated with various sensitivity tests carried out.

761

Simulations	Ice number conc. (cm ⁻³)			LWC (g/m ³)			Downward shortwave radiation flux	Downward longwave radiation flux	Cloud cover (%)	Accumulated surface precipitation (mm)
	<i>Total</i>	<i>Convective</i>	<i>Stratiform</i>	<i>Total</i>	<i>Convective</i>	<i>Stratiform</i>				
control	0.76	0.47	0.052	0.128	0.285	0.063	165.28	136.8	0.231	20.10
no-PBAP	0.72	0.46	0.057	0.13	0.281	0.069	163.42	139.6	0.224	19.92
no-PBAP INP	0.80	0.48	0.053	0.13	0.287	0.068	164.7	137.3	0.229	20.14
high-PBAP	0.71	0.44	0.050	0.14	0.30	0.068	168.1	138.6	0.227	19.96
very high-PBAP	0.73	0.44	0.043	0.135	0.29	0.068	166.07	138.8	0.24	20.04
ultra high-PBAP	0.60	0.48	0.03	0.141	0.29	0.070	159.4	133.1	0.26	20.70
no-sublimation breakup	0.84	0.52	0.054	0.12	0.26	0.065	184.1	144.9	0.21	20.52
No-collisional ice-ice breakup	1.82	1.35	0.21	0.15	0.32	0.082	153.4	123.6	0.24	15.41
No-secondary	1.89	1.45	0.18	0.15	0.30	0.08	158.6	115.7	0.26	24.23
very high-PBAP with no secondary	1.85	1.38	0.20		0.30	0.085	208.3	127.8	0.28	23.95

762 Figure 9 shows the corresponding effects in the stratiform region ($w < 1$ m/s) from all
763 bioaerosols. The changes in warm microphysical properties as a result of changes in PBAP
764 loadings are smaller than 10%. In this part of the cloud, the ice-microphysical parameters are
765 comparatively more sensitive to the changes in PBAP than in the convective region. The ultra
766 high-pbap case predicted ~40% lower ice number concentration than the control run.
767 However, these changes in ice number concentration are not significant as the error bars
768 associated with ensemble members overlap. For the stratiform region, all other simulations
769 considered here showed $< 10\%$ change in ice number concentrations compared to the control
770 run. These changes in ice number concentration due to PBAPs are mostly controlled through
771 their effect on homogeneous freezing above the -36°C level as shown in Figure 9e by tagging
772 tracer for homogeneous nucleation. These ice particles can then advect to lower levels
773 affecting ice number concentrations in the mixed-phase region.

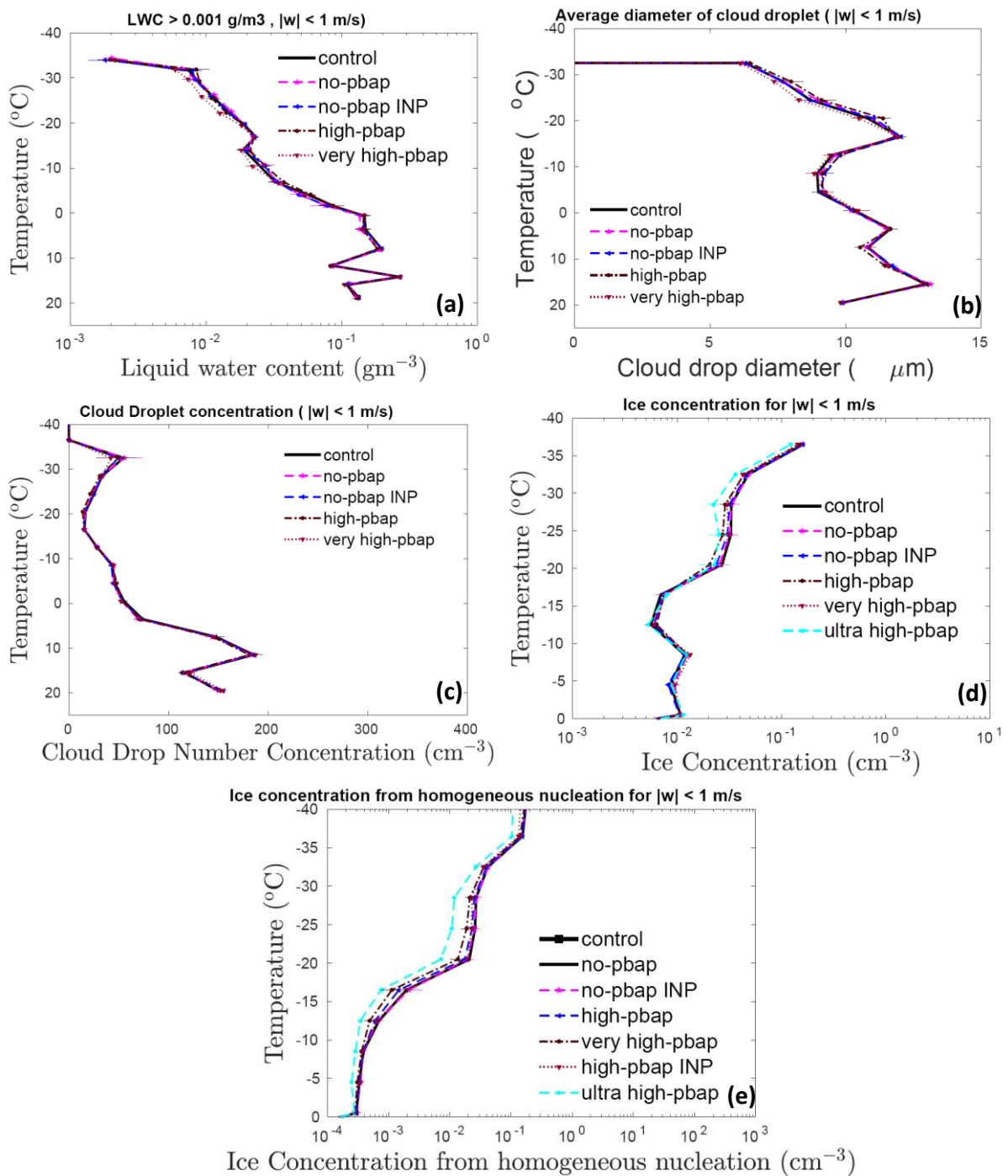
774

775 Figure 10 shows the number of ice particles generated by homogeneous nucleation, various
776 mechanisms of primary nucleation (10a), and secondary ice production (10b) per 10^{15} ice
777 particles for the entire storm. Homogeneous freezing dominates the ice production among the
778 three broad types of ice formation mechanisms (heterogeneous and homogeneous ice
779 nucleation, SIP). The maximum changes in ice nucleated through the primary ice mechanism
780 are noticed for the very high-PBAP case and can be attributed to the 100-fold increase in all
781 PBAP loading. The very high-PBAP simulation predicted a 15% lower number of
782 homogeneously nucleated ice than the control run. The very high-PBAP cases predicted
783 about 80% more primary ice crystals formed at temperatures warmer than -30°C . At
784 temperatures colder than -30°C , this case predicted 20% more primary ice crystals than the
785 control run. The very high pbap case showed an increase in primary heterogeneous ice and a
786 decrease in primary homogenous ice. Since the contribution of primary homogenous ice

787 nucleation is much higher in determining the total ice number concentration when compared
 788 with primary homogeneous nucleation, the overall effect of the very high pbap case is a
 789 decrease in total ice number concentration as shown in Figure 9 and Table 4.

790

791

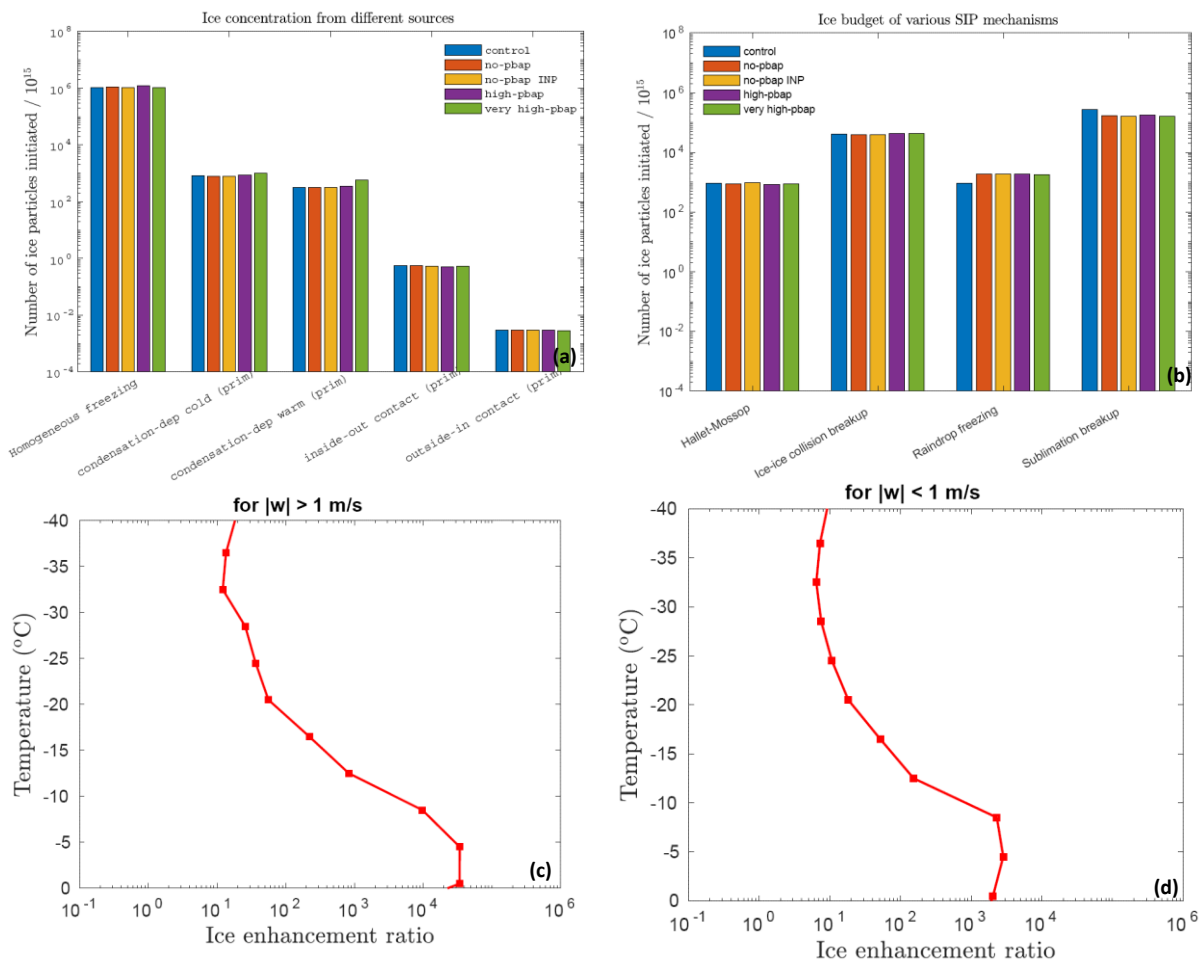


792

793 **Figure 9:** The temperature dependence of (a) the liquid water content, (b) the cloud droplet
 794 number, (c) the cloud droplet diameter, and the (d) total ice number concentration for
 795 ‘control’ simulation and various sensitivity runs involving a change in total PBAP number
 796 concentrations for in the stratiform region. Also shown is the temperature dependence of (e)
 797 ice concentration from homogeneous freezing. The averaging conditions are mentioned at the
 798 top of each figure. The total ice number concentration and ice number from homogeneous
 799 freezing from ultra high-PBAP are also shown in panels d and e. All the vertical profiles
 800 shown here are averaged for the whole domain. The error bars are based in ensemble runs.

801

802



803

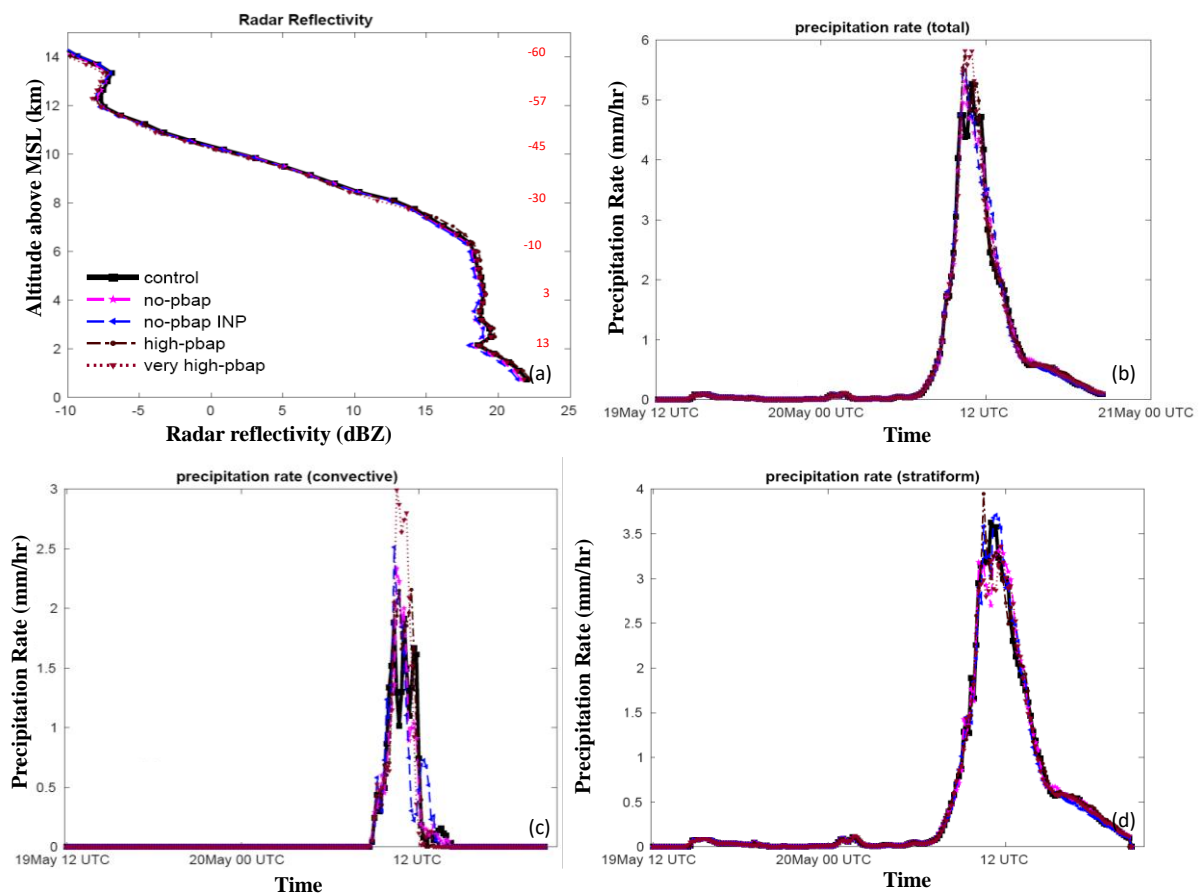
804 **Figure 10:** The number of ice crystals produced during the whole storm by (a) primary ice
 805 nucleation mechanisms and homogeneous freezing as well as (b) various SIP mechanisms (as
 806 shown in the legend box) per 10^{15} particles is shown for various sensitivity runs.

807

808

809 Figure 10b shows that among SIP mechanisms, the contributions of ice-ice collision breakup
 810 and sublimation breakup are higher by an order of magnitude than the HM process and

811 raindrop fragmentation. However, the budget analysis (not shown in the plot) showed that
 812 about 75% of the fragments associated with sublimation breakup are prone to evaporation,
 813 making ice-ice collision breakup a major SIP mechanism. The estimated ice enhancement
 814 ratio, which is a ratio between the number concentrations of total ice (excluding
 815 homogeneous nucleation) and primary ice, is shown in Figures 10c and 10d for convective
 816 and stratiform regions respectively. Overall, the ice enhancement ratio varied between 10 to
 817 10^4 which indicates the importance of SIP mechanisms. The budget analysis shows that
 818 overall, the perturbations in bioaerosols resulted in very small changes (with maximum
 819 change < 40%) in ice generated by SIP mechanisms.



820

821 **Figure 11:** The vertical profiles of (a) radar reflectivity are shown for simulations involving
 822 changes in PBAP. (b) The temporal evolution of the total surface precipitation rate averaged
 823 over the domain is also shown. The time series of surface precipitation rate averaged over the
 824 domain is also shown separately for (c) convective and (d) stratiform regions. All the vertical
 825 profiles shown here are averaged for the whole domain.

826 Figure 11a shows the effects of PBAP on the simulated radar reflectivity for the whole storm.
827 When compared to the control run, there is no significant difference in the simulated radar
828 reflectivity of the perturbed simulations ($< 4\%$). Figure 11b depicts the sensitivity of the total
829 surface precipitation rate averaged over the domain to the changes in total PBAPs. As shown
830 in Figure 11b, the peak in surface precipitation rate is boosted by about 10% in the very high-
831 PBAP cases compared to the control run. In remaining perturbed simulations, changes in
832 surface precipitation rate are less than 5% when compared with the control run. The
833 contribution from the stratiform component of rain is higher in the total amount of rain (90%)
834 as compared to the convective rain (remaining 10%) (see Fig. 11c and 11d). Convective
835 rainfall is more sensitive to the changes in PBAPs than stratiform rainfall. The increase in
836 PBAPs by 100-fold results in a 50% higher peak of convective rainfall rate as compared to
837 the control run.

838

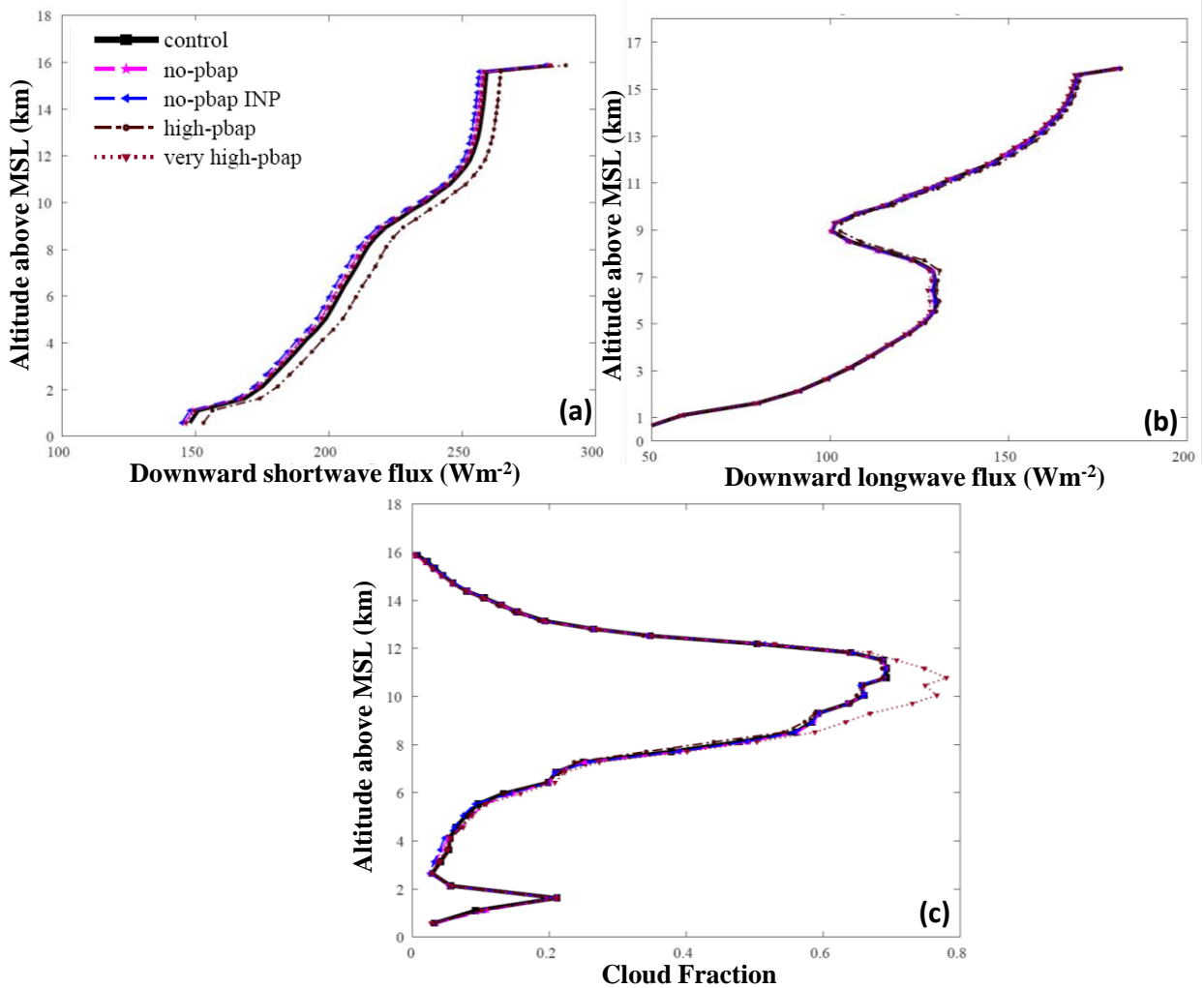
839 The changes in accumulated surface precipitation due to PBAPs are shown in Table 4. The
840 spatial distribution of accumulated surface rainfall shows considerable variation associated
841 with changes in PBAPs (Figure S7). However, the overall effect of PBAPs on accumulated
842 surface precipitation is minimal ($< 4\%$).

843

844

845 Figure 12 shows the domain averaged vertical profiles of shortwave, longwave fluxes, and
846 cloud fractions for the different sensitivity tests considered here. Among all the sensitivity
847 runs, only the high-PBAP case showed a noticeable effect on shortwave flux, which was 2%
848 higher than the control run. The variations in longwave fluxes were less than 1%. The vertical
849 profiles of cloud fraction show that a 100-fold increase in total PBAPs results in a 10%
850 higher cloud fraction between 8 and 12 km. However, the overall change in cloud fraction

851 from 100-fold increase in PBAP is less than 4% as shown in Table 4. The cloud fraction in
 852 other sensitivity runs was less sensitive to the changes in PBAP loadings. The ultra high-pbap
 853 case simulated a predicted 10% higher cloud fraction than the control run (see Table 4)
 854



855
 856 **Figure 12:** The domain averaged vertical profiles of downward components of (a) shortwave
 857 flux, (b) longwave flux, and (c) cloud fraction for various sensitivity experiments. The data
 858 shown here is an unconditional average over the whole duration and domain of each
 859 simulation. All the vertical profiles shown here are averaged for the whole domain.

860
 861
 862
 863

864 **6. Results from sensitivity tests about secondary ice production**

865 Various sensitivity experiments were conducted to evaluate the role of SIP mechanisms in
866 determining micro- and macrophysical parameters of the clouds. SIP through sublimation
867 breakup and breakup in ice-ice collisions were switched off in the 'no-sublimation breakup'
868 and 'no-collisional ice-ice breakup' simulations, respectively. In the 'no-secondary' case, no
869 SIP mechanisms were active.

870

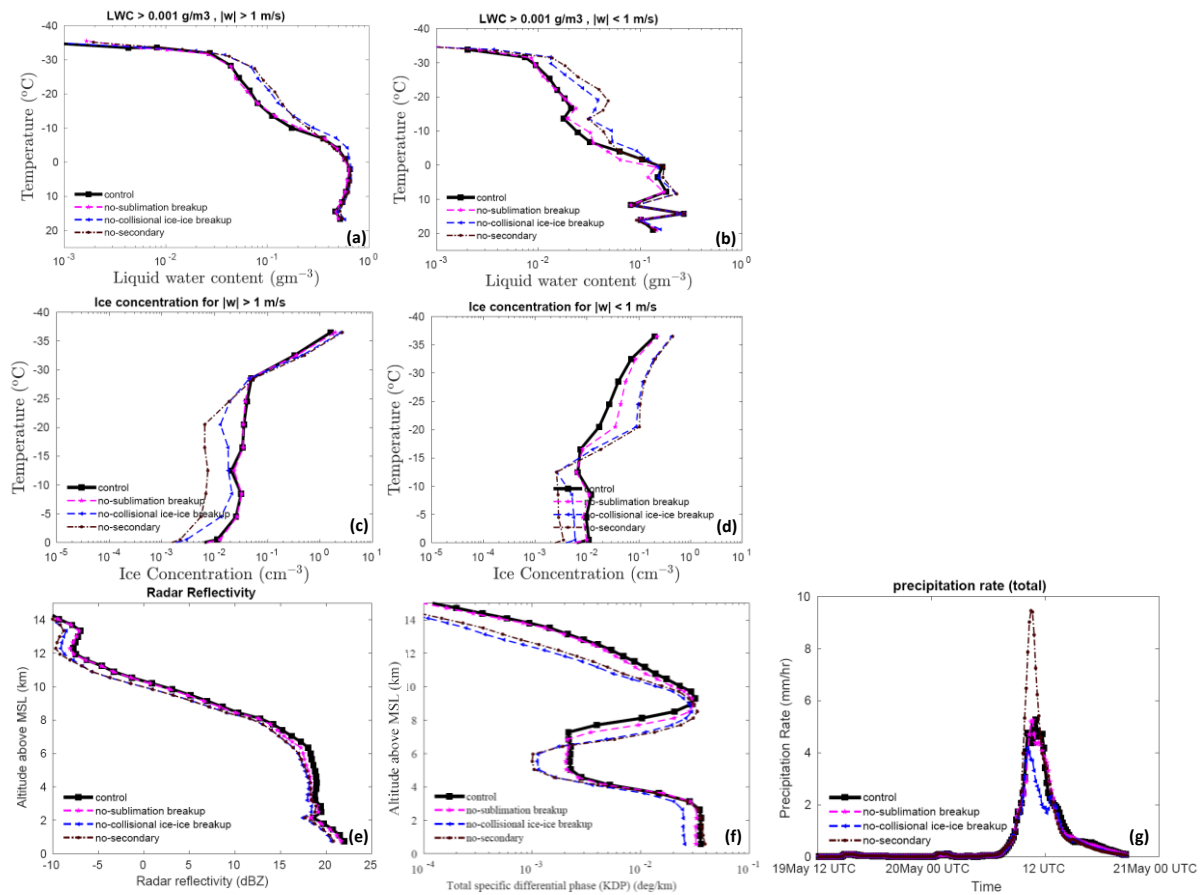
871 The results from these sensitivity experiments are shown in Figure 13 for the convective as
872 well as the stratiform region of the simulated cloud. Overall, in the convective region, the no-
873 secondary and no-collisional ice-ice breakup cases predicted 5 and 12% higher LWC
874 respectively, than the control run (See Table 4). In the stratiform region, these cases predicted
875 ~25% higher LWC than the control run. Lower ice number concentrations due to the absence
876 of SIP mechanisms may reduce the rate of conversion of liquid to ice via mixed-phase
877 processes, resulting in a higher LWC.

878

879 In the convective part, the absence of any SIP increased ice number concentration by half an
880 order of magnitude at temperatures warmer than -25°C . Comparing the no-SIP and control
881 cases, the effect of the inclusion of SIP mechanisms is to increase the average ice
882 concentration by up to half an order of magnitude at temperatures warmer than -15°C in the
883 stratiform region. For the stratiform region, at temperatures colder than this, the absence of
884 SIP mechanisms resulted in higher ice number concentrations by a similar magnitude. These
885 changes at the colder levels are associated with homogeneous droplet freezing. The changes
886 in ice number concentration in the no-collisional ice-ice breakup case are comparable with
887 the no-secondary case. Compared to break up in ice-ice collisions, sublimation breakup has a

888 lower impact ($< 40\%$) on the total ice number concentration in both convective and stratiform
 889 regions.

890



891

892 **Figure 13:** Temperature dependence of the liquid water content in (a) the convective and
 893 (b) the stratiform region for ‘control’ simulation and various sensitivity runs involving SIPs.
 894 The ice number concentration is also shown for the (c) convective and (d) stratiform regions.
 895 The averaging conditions are mentioned at the top of each figure. The vertical profiles of (e)
 896 radar reflectivity, (f) total specific differential phase are also shown for the same simulations.
 897 (g) The temporal evolution of the total surface precipitation rate averaged over the domain is
 898 also shown. All the vertical profiles shown here are averaged for the whole domain.

899

900

901 The changes in simulated radar reflectivity, total specific differential phase, and surface
 902 precipitation rate with SIP mechanisms are shown in Figures 13e, 13f, and 13g, respectively

903 for the whole storm. Overall, the simulated radar reflectivity was 1 dBZ lower in the no-SIP
904 and no-collisional ice-ice breakup case than in the control run and can be attributed to the
905 overall increase in ice number concentration in the control run. The no-sublimation case
906 predicted slightly higher reflectivity than the control run. The absence of all SIPs resulted in
907 about a 100% decrease in the K_{DP} at a temperature colder than -40°C . Between -10°C to -
908 30°C , the absence of no-collisional breakup and no-secondary resulted in higher K_{DP} (half an
909 order of magnitude) values than the control run. The absence of all SIP mechanisms results in
910 a higher surface precipitation rate (75%) during the peak rainfall hour, which occurs around
911 11.30 UTC compared to the control run. In the previous study, Phillips et al. (2017) have
912 shown that SIP through ice-ice collision breakup can reduce accumulated surface
913 precipitation in the simulated storm by 20%-40%. They attributed it to the increase in snow
914 particles competing for available liquid and the reduction in their growth by riming. It
915 resulted in smaller ice particles and a reduction in surface precipitation.

916

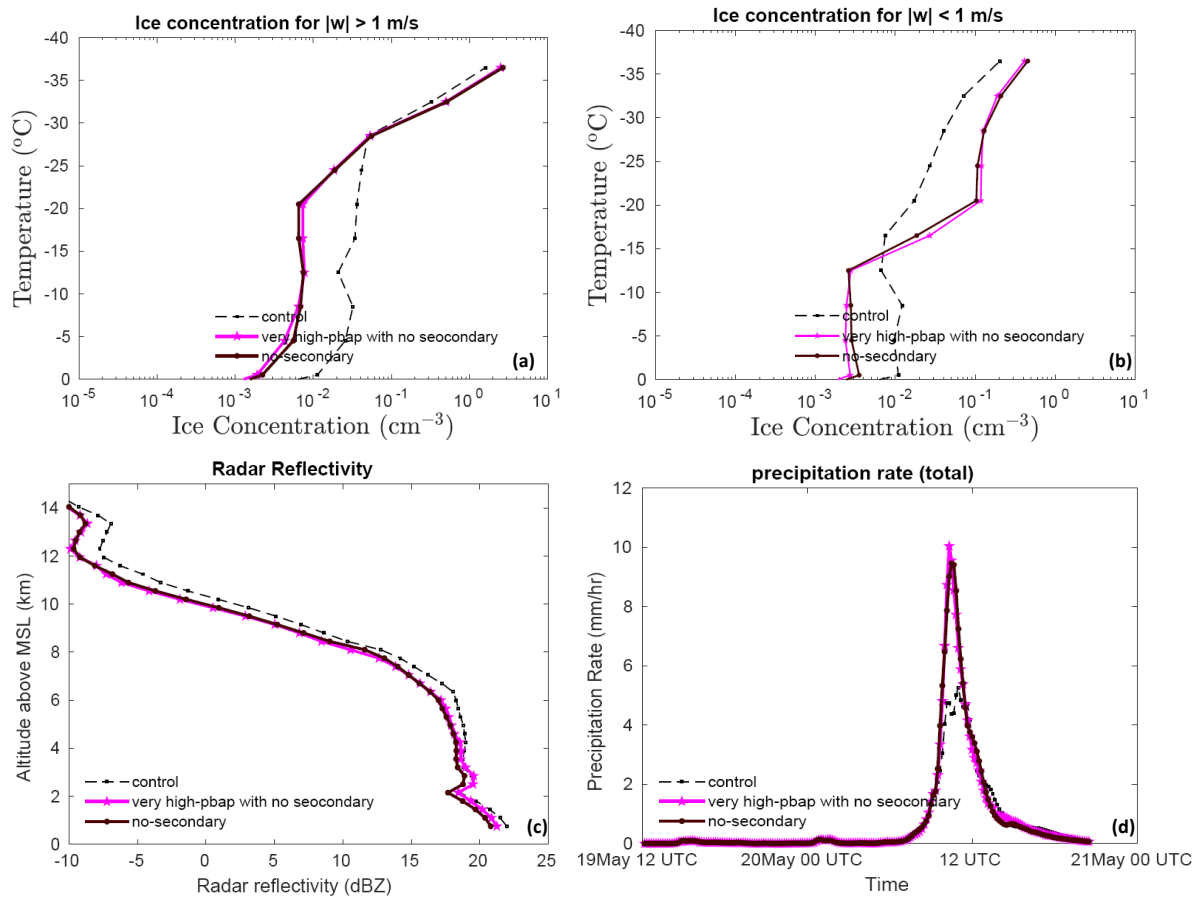
917

918 **7. Results about the influence of PBAPs in the absence of SIP mechanisms**

919 Most SIP mechanisms are highly active at temperatures above -15°C . The majority of PBAP
920 showed high ice nucleation activity occurs in this part of the cloud. Most of the ice
921 concentration in this part of the cloud is determined by various SIP mechanisms. Thus, the
922 SIP mechanisms may influence the role of PBAPs in altering cloud microphysical properties.
923 To investigate this aspect, an additional simulation was performed by eliminating all
924 secondary ice processes from the control run and multiplying the initial loading of all PBAP
925 groups by a factor of 100 (the '*very high-PBAP with no SIP*' case). The results of this
926 simulation are then compared to the no-SIP case as shown in Figure 14.

927

928 In the absence of any SIP mechanisms, the 100-fold increase in bioaerosols resulted in
929 minimal effect on ice number concentration. Overall, without SIP the increase in bioaerosol
930 loading by 100-fold resulted in less than a 5% change in ice number concentration. This
931 indicates that the ice produced by various SIP mechanisms does not alter the effect of
932 bioaerosols on-ice number concentration in the simulated clouds. The changes in simulated
933 radar reflectivity due to a 100-fold increase in bioaerosols are negligible ($< 0.5\%$) (Figure
934 14c). The difference in predicted surface precipitation rate and accumulated precipitation
935 between very high-PBAP with no-secondary and no-secondary cases was lower than 3%.



936

937 **Figure 14:** The temperature dependence of ice number concentration for the control, very
938 high-PBAP with no SIP and no-SIP simulations averaged for (a) convective and (b)
939 stratiform regions. The (c) vertical profile of radar reflectivity and the temporal evolution of
940 (d) surface precipitation rate is shown for the entire simulation. All the vertical profiles

941 shown here are averaged for the whole domain. All the vertical profiles shown here are
942 averaged for the whole domain.

943

944

945 **8. Discussion**

946 Five PBAP groups have been implemented in the mesoscale AC model to predict their ice
947 nucleation activity based on the empirical formulation by PT21. The simulated concentrations
948 of major PBAPs including fungi and bacteria are of the same order of magnitude as results
949 from previous modeling studies (Després et al., 2012; Hoose et al., 2010b). Still, the relative
950 abundance of PBAP groups over the simulated region is unknown due to the lack of
951 measurements. The AC model was run with higher resolution (2 X 2 km) compared to
952 previous studies on a global scale (Hoose et al., 2010b), to investigate the potential impact of
953 variations in PBAP concentration on the properties of simulated squall line events more
954 clearly.

955

956 Yet the control simulation is not perfectly accurate in all respects. In the stratiform region
957 between -10 and -16°C, the predicted ice number concentration was lower than observed by
958 aircraft by half an order of magnitude and in a fair agreement at temperatures warmer than -
959 10°C. This uncertainty factor is similar to the uncertainty in the measurements due to various
960 biases (e.g., Field et al. 2006). Nevertheless, all other simulated cloud microphysical
961 parameters, radar reflectivity, and surface precipitation rate were in acceptable agreement
962 with aircraft and ground-based observations.

963

964 In the control simulation, the average ice concentration above the -30°C and -18°C levels is
965 dominated by downwelling of homogeneously nucleated ice from above the mixed-phase
966 region in convective and stratiform clouds respectively. Below both levels, SIP prevails. Both
967 processes of ice initiation (homogeneous freezing and SIP) have only weak sensitivity to
968 PBAPs, hence the weakness of the impact on simulated cloud glaciation.

969

970 Based on the sensitivity experiments, it can be concluded that PBAP INPs have only a limited
971 effect on the average state of the ice phase of the simulated clouds of this mesoscale
972 convective system. Most of the changes in ice number concentration associated with changes
973 in PBAPs are controlled by their effects on homogeneous nucleation and SIPs. The lower
974 dependence of simulated ice number concentration on changes in PBAPs is consistent with
975 the findings of Hummel *et al.* (2018). Based on ensemble simulations of the regional
976 atmospheric model for Europe, they showed that the changes in average ice crystal
977 concentration by biological INPs are very small and are not statistically significant, implying
978 that PBAPs play only a minor role in altering the cloud ice phase. The limited effect of
979 PBAPs on cloud properties on a global scale has been highlighted in previous studies (Hoose
980 *et al.*, 2010b; Sesartic *et al.*, 2012, 2013; Spracklen and Heald, 2014).

981

982 The weakness of the simulated impact from realistic PBAP fluctuations is explicable mostly
983 in terms of the low contribution from biological ice nucleation compared to non-biological
984 INPs to overall ice initiation. In terms of ice nucleation efficiency and onset temperatures,
985 each PBAP group has different ice nucleation properties. Based on vertical profiles of active
986 INPs (Figures 6), the overall contribution of activated INPs from all PBAP groups to the total
987 active INPs was $\sim 1\%$. At -15°C , temperature, the active INPs from dust and black carbon was

988 one order higher than PBAP INPs. At -30°C, the predicted INPs from dust and black carbon
989 were higher by one and two orders of magnitude, respectively, than PBAP INPs. The dust
990 and black carbon INPs activated at these temperatures can be advected down to the levels
991 where PBAP INPs are most important. Overall, this resulted in low sensitivity of the average
992 ice phase to the changes in bioaerosol loading.

993

994 The ice production in the simulated cloud system at levels in the mixed-phase region (0 to -36
995 °C) is largely controlled by various SIP mechanisms of which the most important is the
996 breakup in ice-ice collisions. Some of these processes are active at temperatures warmer than
997 -15°C (e.g., the HM process) where PBAP INP are important and expected to enhance the
998 biological ice nucleation. However, our results showed that the ice production associated with
999 SIP mechanisms is less sensitive to the initial PBAP loading because SIP causes positive
1000 feedback of ice multiplication with ice fragments growing to become precipitation-size
1001 particles that then fragment again.

1002

1003 In our study, 100-fold increase in PBAPs leads to a < 4% change in surface precipitation.
1004 Using mesoscale model simulations, Phillips et al. (2009) reported a 10% increase in
1005 accumulated surface precipitation associated with deep convective clouds due to a 100-fold
1006 increase in biological particles. Phillips et al. (2009) also noted an effect (up to 4%) on
1007 surface shortwave and TOA longwave radiation flux because of changes in PBAP number
1008 concentration. In our study, the changes in PBAP loading caused smaller changes in
1009 simulated shortwave and longwave fluxes (< 3%). Sesartic et al. (2012, 2013) showed that
1010 including fungi and bacteria in the global climate model leads to minor changes (< 0.5%) in
1011 the ice water path, total cloud cover, and total precipitation.

1012

1013 It should be noted that the sensitivity experiments carried out in the current study are limited
1014 to the small domain (80 X 80 km domain) representing a limited area of the global
1015 ecosystem. Also, the model top was located at 16 km, and it may not represent the whole
1016 atmosphere. The results presented here are based on a mesoscale model and may not
1017 represent the global impact of PBAPs on clouds.

1018

1019

1020 **9. Conclusions**

1021 A framework describing the ice nucleation activity of five major groups of PBAPs including
1022 fungal spores, bacteria, pollen, viral particles, plant/animal detritus, algae, and their
1023 respective fragments was provided by PT21. The ice nucleation activity of these major PBAP
1024 groups in the EP was based on samples from the real atmosphere. The present study
1025 implements this EP in AC and investigates the role of these five PBAP groups as INPs in
1026 deep convective clouds. The high-resolution (2 km horizontally) simulations over a
1027 mesoscale 3D domain (80 km wide) using AC elucidate the impact of these PBAP groups on
1028 the cloud properties. A series of sensitivity experiments were conducted to test the impact of
1029 PBAP groups on cloud properties.

1030

1031 A mid-latitude squall line that occurred on 20 May 2011 during MC3E over the US Southern
1032 Great Plains is simulated with the model. The simulated number concentration of ice particles
1033 showed good agreement (to within about 50%) with aircraft observations for the convective
1034 clouds within the mesoscale system. In the stratiform region between -10 and -16°C, the

1035 model predicted ice number concentration was lower than the aircraft observation by half an
1036 order of magnitude and in a fair agreement at temperatures warmer than -10°C . Various
1037 sensitivity experiments were carried out by perturbing the initial PBAP loading and by
1038 altering various SIP mechanisms.

1039

1040 Each PBAP group has diverse properties including its shape, size, and abundance in the
1041 atmosphere. A small fraction of PBAPs is found to be ice nucleation active and can therefore
1042 act as PBAP INPs. The relative contribution of each PBAP within the total PBAPs may vary
1043 from one ecosystem to another. In the current study, their relative contribution is based on
1044 previous observations from Amazonia and can be considered as the main limitations of this
1045 study. However, the simulated number concentrations of major PBAPs including fungi, and
1046 bacteria look reasonable and are close to their typical abundance in the atmosphere.

1047

1048 Any perturbation in the PBAP concentration by factors upto 1000 assumed in the current
1049 study (resulted in maximum changes in ice number concentration by $< 6\%$ convective region
1050 and by $< 40\%$ in the stratiform region with respect to the control run. The simulations showed
1051 that simulated ice particle number concentration is much higher than the number
1052 concentrations of PBAP INPs. Even at temperatures warmer than -15°C , where PBAP INPs
1053 are thought to be the most important INP, ice crystals originated from primary heterogeneous
1054 nucleation of dust and black carbon from higher levels of the cloud frequently perturb the
1055 lower levels due to sedimentation. The major ice formation comes from SIP mechanisms and
1056 homogeneous nucleation, both are less sensitive to the changes in PBAPs. Therefore, PBAP
1057 INPs do not show a significant impact on the average ice phase of the simulated storm.

1058

1059 PBAPs have minimal effect on the warm microphysical properties of simulated clouds. The
1060 effect on liquid water content and cloud droplet number concentration was lower than 10% in
1061 both convective and stratiform regions. Since both ice and warm microphysical processes are
1062 less sensitive to PBAPs, surface precipitation is not affected significantly by changes in
1063 PBAPs. A 100-fold increase in all PBAPs resulted in less than a 5% change in surface
1064 precipitation.

1065

1066

1067

1068

1069

1070

1071

1072

1073

1074

1075

1076

1077

1078

1079

1080 **Code and data availability:** Data and the code for the empirical formulation of PBAPs are
1081 available on request by contacting the corresponding author.

1082 **Competing interests:** The authors declare no conflict of interest

1083 **Author Contributions:** VJTP designed and monitored this study. SP conducted model
1084 simulation, most of the data analysis, and wrote the initial manuscript. All authors contributed
1085 to the scientific discussion and model development.

1086 **Financial support:** This work was completed for a sub-award (award number: 2019-26-03)
1087 to VTJP from a US Department of Energy (DoE) direct grant to the Ryzhkov at the
1088 University of Oklahoma (award number: DE-SC0018967). The first author was also
1089 supported by a past award from the Swedish Research Council ('VR'), which concerns
1090 modeling bio-aerosol effects on glaciated clouds (2015-05104) and Sweden's Innovation
1091 Agency (Vinnova; 2020-03406). Other co-authors were supported by a current award from
1092 the Swedish Research Council for Sustainable Development (FORMAS; award number
1093 2018-01795) and US Department of Energy Atmospheric Sciences Research Program (award
1094 number: DE-SC0018932).

1095

1096

1097

1098

1099

1100

1101

1102 **References:**

- 1110 Blyth AM, Latham J. 1993. Development of ice and precipitation in New Mexican
1111 summertime cumulus clouds. *Q. J. R. Meteorol. Soc.* 119:91–120
- 1112 Baumgardner, D., Abel, S. J., Axisa, D., Cotton, R., Crosier, J., Field, P., Gurganus, C.,
1113 Heymsfield, A., Korolev, A., Krämer, M., Lawson, P., McFarquhar, G., Ulanowski, Z.,
1114 & Um, J. (2017). Cloud Ice Properties: In Situ Measurement Challenges, *Meteorological*
1115 *Monographs*, 58, 9.1-9.23.
- 1116 Bowers RM, Lauber CL, Wiedinmyer C, Hamady M, Hallar AG, Fall R, Knight R, Fierer N.
1117 Characterization of airborne microbial communities at a high-elevation site and their
1118 potential to act as atmospheric ice nuclei. *Appl Environ Microbiol.* 2009
1119 Aug;75(15):5121-30. doi: 10.1128/AEM.00447-09
- 1120 Bauer, H., Kasper-Giebl, A., Loflund, M., Giebl, H., Hitzenberger, R., Zibuschka, F., and
1121 Puxbaum, H.: The contribution of bacteria and fungal spores to the organic carbon
1122 content of cloud water, precipitation and aerosols, *Atmos. Res.*, 64, 109–119, 2002.
- 1123 Burrows, S. M., Elbert, W., Lawrence, M. G., and Pöschl, U.: Bacteria in the global
1124 atmosphere – Part 1: Review and synthesis of literature data for different ecosystems,
1125 *Atmos. Chem. Phys.*, 9, 9263–9280
- 1126
- 1127 Carlin, J. T., Reeves, H. D., & Ryzhkov, A. V. 2021: Polarimetric Observations and
1128 Simulations of Sublimating Snow: Implications for Nowcasting, *Journal of Applied*
1129 *Meteorology and Climatology*, 60(8), 1035-1054.
- 1130 Chen, Q., Yin, Y., Jiang, H., Chu, Z., Xue, L., Shi, R., et al. (2019). The roles of mineral dust
1131 as cloud condensation nuclei and ice nuclei during the evolution of a hail storm. *Journal*
1132 *of Geophysical Research: Atmospheres*, 2019; 124: 14262– 14284.
- 1133 Chin, M., R. B. Rood, S. J. Lin, J. F. Müller, and A. M. Thompson, 2000: Atmospheric sulfur
1134 cycle simulated in the global model GOCART: Model description and global properties.
1135 *Journal of Geophysical Research Atmospheres*, **105**, 24671–24687,
1136 <https://doi.org/10.1029/2000JD900384>.
- 1137 Crawford, I., Bower, K. N., Choullarton, T. W., Dearden, C., Crosier, J., Westbrook, C.,
1138 Capes, G., Coe, H., Connolly, P. J., Dorsey, J. R., Gallagher, M. W., Williams, P.,
1139 Trembath, J., Cui, Z., and Blyth, A.: Ice formation and development in aged, wintertime
1140 cumulus over the UK: observations and modelling, *Atmos. Chem. Phys.*, 12, 4963–
1141 4985, <https://doi.org/10.5194/acp-12-4963-2012>, 2012.
- 1142 Cui, Z., and K. S. Carslaw , 2006: Enhanced vertical transport efficiency of aerosol in
1143 convective clouds due to increases in tropospheric aerosol abundance, *J. Geophys. Res.*,
1144 111, D15212, doi:10.1029/2005JD006781
- 1145 Deshmukh A., Vaughan T. J. Phillips, Aaron Bansemmer, Sachin Patade, and Deepak Waman,
1146 2021: New Empirical Formulation for the Sublimational Breakup of Graupel and
1147 Dendritic Snow, DOI: <https://doi.org/10.1175/JAS-D-20-0275.1>

1148 Després, V. R., and Coauthors, 2012: Primary biological aerosol particles in the atmosphere:
1149 A review. *Tellus, Series B: Chemical and Physical Meteorology*, **64**,
1150 <https://doi.org/10.3402/tellusb.v64i0.15598>.

1151 DeMott P. J., A.J. Prenni, X. Liu, S.M. Kreidenweis, M.D. Petters, C.H. Twohy, *et al.*
1152 Predicting global atmospheric ice nuclei distributions and their impacts on climate Proc.
1153 Natl. Acad. Sci. U. S. A., 107 (2010), pp. 11217-11222.

1154 DeMott, P. J. and Prenni, A. J.: New Directions: Need for defining the numbers and sources
1155 of biological aerosols acting as ice nuclei, *Atmos. Environ.*, 44, 1944–1945, 2010.

1156 Després, V.R., Huffman, J.A., Burrows, S.M., Hoose, C., Safatov, A.S., Buryak, G.,
1157 Fröhlich-Nowoisky, J., Elbert, W., Andreae, M.O., Pöschl, U., 2012. Primary
1158 biological aerosol particles in the atmosphere: a review. *Tellus B Chem. Phy.*
1159 *Meteorol.* 64 (1), 15598.

1160 Dong, X., and G. G. Mace, 2003: Arctic stratus cloud properties and radiative forcing derived
1161 from ground-based data collected at Barrow, Alaska. *J. Climate*, **16**, 445–461,
1162 doi:10.1175/1520-0442(2003)016<0445:ASCPAR>2.0.CO;2.

1163 Han, B., Fan, J., Varble, A., Morrison, H., Williams, C. R., Chen, B., et al. (2019). Cloud-
1164 resolving model intercomparison of an MC3E squall line case: Part II. Stratiform
1165 precipitation properties. *Journal of Geophysical Research: Atmospheres*, 124, 1090–
1166 1117.

1167 Fan, J, Liu, Y-C, Xu, K-M, North, K, Collis, S, Dong, X, Zhang, GJ, Chen, Q, Kollias, P, and
1168 Ghan, SJ (2015), Improving representation of convective transport for scale-aware
1169 parameterization: 1. Convection and cloud properties simulated with spectral bin and
1170 bulk microphysics. *J. Geophys. Res. Atmos.*, 120, 3485– 3509. doi:
1171 10.1002/2014JD022142.

1172 Fan J., J.M. Comstock, M. Ovchinnikov, 2010: The cloud condensation nuclei and ice nuclei
1173 effects on tropical anvil characteristics and water vapor of the tropical tropopause layer
1174 *Environ. Res. Lett.*, 5 (2010), Article 044005, 10.1088/1748-9326/5/4/044005

1175 Fan J., Bin Han, Adam Varble, Hugh Morrison, Kirk North, Pavlos Kollias, Baojun Chen,
1176 Xiquan Dong, Scott E. Giangrande, Alexander Khain, Yun Lin, Edward Mansell, Jason
1177 A. Milbrandt, Ronald Stenz, Gregory Thompson, Yuan Wang, 2017: Cloud-resolving
1178 model intercomparison of an MC3E squall line case: Part I—Convective updrafts, *J.*
1179 *Geophys. Res. Atmos.*, 122, 9351– 9378

1180 Field, P. R., and A. J. Heymsfield (2015): Importance of snow to global precipitation, *Geo-*
1181 *phys. Res. Lett.*, 42, 9512–9520,doi:10.1002/2015GL065497.

1182 Field, P. R., Heymsfield, A. J., & Bansemer, A. (2006). Shattering and Particle Interarrival
1183 Times Measured by Optical Array Probes in Ice Clouds, *Journal of Atmospheric and*
1184 *Oceanic Technology*, 23(10), 1357-1371.

1185 Fridlind, A. M., and Coauthors, 2017: Derivation of aerosol profiles for MC3E convection
1186 studies and use in simulations of the 20 May squall line case. *Atmospheric Chemistry*
1187 *and Physics*, **17**, 5947–5972, <https://doi.org/10.5194/acp-17-5947-2017>.

1188 Fröhlich-Nowoisky, J., Kampf, C.J., Weber, B., Huffman, J.A., Pöhlker, C., Andreae, M.
1189 O., Lang-Yona, N., Burrows, S.M., Gunthe, S.S., Elbert, W., Su, H., Hoor, P.,
1190 Thines, E., Hoffmann, T., Després, V.R., Pöschl, U., 2016. Bioaerosols in the Earth
1191 system: climate, health, and ecosystem interactions. *Atmos. Res.* 182, 346–376.

1192 Garcia, E., T. C. J. Hill, A. J. Prenni, P. J. DeMott, G. D. Franc, and S. M. Kreidenweis,
1193 2012: Biogenic ice nuclei in boundary layer air over two US high plains agricultural
1194 regions. *Journal of Geophysical Research Atmospheres*, **117**, 1–12,
1195 <https://doi.org/10.1029/2012JD018343>.

1196 Giangrande, S. E., S. Collis, A. K. Theisen, and A. Tokay, 2014: Precipitation estimation
1197 from the ARM distributed radar network during the MC3E campaign. *Journal of*
1198 *Applied Meteorology and Climatology*, **53**, 2130–2147, [https://doi.org/10.1175/JAMC-](https://doi.org/10.1175/JAMC-D-13-0321.1)
1199 [D-13-0321.1](https://doi.org/10.1175/JAMC-D-13-0321.1).

1200 Grützun, V., O. Knöth, and M. Simmel, 2008: Simulation of the influence of aerosol particle
1201 characteristics on clouds and precipitation with LM-SPECS: Model description and first
1202 results. *Atmospheric Research*, **90**, 233–242,
1203 <https://doi.org/10.1016/j.atmosres.2008.03.002>.

1204 Hallett, J., and S. C. Mossop, 1974: Production of secondary ice particles during the riming
1205 process. *Nature*, 249, 26–28, <https://doi.org/10.1038/249026a0>.

1206 Heymsfield, A. J., Schmitt, C., Chen, C., Bansemer, A., Gettelman, A., Field, P. R., & Liu, C.
1207 (2020). Contributions of the Liquid and Ice Phases to Global Surface Precipitation:
1208 Observations and Global Climate Modeling, *Journal of the Atmospheric Sciences*, 77(8),
1209 2629-2648

1210 Hoose, C., and O. Möhler, 2012: Heterogeneous ice nucleation on atmospheric aerosols: A
1211 review of results from laboratory experiments. *Atmospheric Chemistry and Physics*, **12**,
1212 9817–9854, <https://doi.org/10.5194/acp-12-9817-2012>.

1213 Hoose, C., J. E. Kristjánsson, and S. M. Burrows, 2010: How important is biological ice
1214 nucleation in clouds on a global scale? *Environmental Research Letters*, **5**,
1215 <https://doi.org/10.1088/1748-9326/5/2/024009>.

1216 Hoose, C., Kristjánsson, J. E., Chen, J.-P., and Hazra, A.: A Classical-Theory-Based
1217 Parameterization of Heterogeneous Ice Nucleation by Mineral Dust, Soot, and
1218 Biological Particles in a Global Climate Model, *J. Atmos. Sci.*, 67, 2483–
1219 2503, <https://doi.org/10.1175/2010jas3425.1>, 2010b.

1220 Huang S., Wei Hu, Jie Chen, Zhijun Wu, Daizhou Zhang, Pingqing Fu, Overview of
1221 biological ice nucleating particles in the atmosphere, *Environment International*,
1222 Volume 146, 2021,106197

- 1223 Huffman, J. A., and Coauthors, 2013: High concentrations of biological aerosol particles and
 1224 ice nuclei during and after rain. *Atmospheric Chemistry and Physics*, **13**, 6151–6164,
 1225 <https://doi.org/10.5194/acp-13-6151-2013>.
- 1226 Hummel, M., C. Hoose, B. Pummer, C. Schaupp, J. Fröhlich-Nowoisky, and O. Möhler,
 1227 2018: Simulating the influence of primary biological aerosol particles on clouds by
 1228 heterogeneous ice nucleation. *Atmospheric Chemistry and Physics*, **18**, 15437–15450,
 1229 <https://doi.org/10.5194/acp-18-15437-2018>.
- 1230 Jensen, M. P., and Coauthors, 2016: The midlatitude continental convective clouds
 1231 experiment (MC3E). *Bulletin of the American Meteorological Society*, **97**, 1667–1686,
 1232 <https://doi.org/10.1175/BAMS-D-14-00228.1>.
- 1233 Jaenicke, R., 2005. Abundance of cellular material and proteins in the atmospheric. *Science*
 1234 **308**, 73.
- 1235 Kanji, Z. A., Ladino, L. A., Wex, H., Boose, Y., Burkert-Kohn, M., Cziczo, D. J., & Krämer,
 1236 M. (2017). Overview of Ice Nucleating Particles, *Meteorological Monographs*, **58**, 1.1-
 1237 1.33.
- 1238 Korolev, A. V., Kuznetsov, S. V., Makarov, Y. E., & Novikov, V. S. (1991). Evaluation of
 1239 Measurements of Particle Size and Sample Area from Optical Array Probes, *Journal of*
 1240 *Atmospheric and Oceanic Technology*, **8**(4), 514-522.
- 1241 Korolev, A. V., Emery, E. F., Strapp, J. W., Cober, S. G., Isaac, G. A., Wasey, M., &
 1242 Marcotte, D. (2011). Small Ice Particles in Tropospheric Clouds: Fact or Artifact?
 1243 Airborne Icing Instrumentation Evaluation Experiment, *Bulletin of the American*
 1244 *Meteorological Society*, **92**(8), 967-973
- 1245 Korolev, A., McFarquhar, G., Field, P. R., Franklin, C., Lawson, P., Wang, Z., Williams, E.,
 1246 Abel, S. J., Axisa, D., Borrmann, S., Crosier, J., Fugal, J., Krämer, M., Lohmann, U.,
 1247 Schlenczek, O., Schnaiter, M., & Wendisch, M. (2017). Mixed-Phase Clouds: Progress
 1248 and Challenges, *Meteorological Monographs*, **58**, 5.1-5.50
- 1249 Korolev, A. and Leisner, T.: Review of experimental studies of secondary ice production,
 1250 *Atmos. Chem. Phys.*, **20**, 11767–11797, <https://doi.org/10.5194/acp-20-11767-2020>,
 1251 2020.
- 1252 Korolev, A., Heckman, I., Wolde, M., Ackerman, A. S., Fridlind, A. M., Ladino, L. A.,
 1253 Lawson, R. P., Milbrandt, J., and Williams, E.: A new look at the environmental
 1254 conditions favorable to secondary ice production, *Atmos. Chem. Phys.*, **20**, 1391–1429,
 1255 <https://doi.org/10.5194/acp-20-1391-2020>, 2020.
- 1256 Kumjian, M. R., and K. A. Lombardo, 2017: Insights into the evolving microphysical and
 1257 kinematic structure of northeastern U.S. winter storms from dual-polarization Doppler
 1258 radar. *Mon. Wea. Rev.*, **145**, 1033–1061, <https://doi.org/10.1175/MWR-D-15-0451.1>.
- 1259 Knopf, D.A., Alpert, P.A., Wang, B., Aller, J.Y., 2011. Stimulation of ice nucleation by
 1260 marine diatoms. *Nat. Geosci.* **4**, 88–90. <https://doi.org/10.1038/ngeo1037>

- 1261 Lawson, R. P., Woods, S. and Morrison, H., 2015: The microphysics of ice and precipitation
 1262 1195 development in tropical cumulus clouds, *J. Atmos. Sci.*, 72(6), 2429–2445, 1196
 1263 doi:10.1175/JAS-D-14-0274.1, 2015.
- 1264 Levin Z, Yankofsky S, Pardes D and Magal N, 1987, *J. Clim. Appl. Meteorol.* 26 1188–97
- 1265 Matus, A. V. and L'Ecuyer, T. S. (2017), The role of cloud phase in Earth's radiation budget,
 1266 *J. Geophys. Res. Atmos.*, 122, 2559– 2578, doi:10.1002/2016JD025951.
- 1267 Malm, W. C., J. F. Sisler, D. Huffman, R. A. Eldred, and T. A. Cahill (1994), Spatial and
 1268 seasonal trends in particle concentration and optical extinction in the United States, *J.*
 1269 *Geophys. Res.*, 99, 1347-1370.
- 1270 Matthias-Maser S., Berit Bogs, Ruprecht Jaenicke, The size distribution of primary biological
 1271 aerosol particles in cloud water on the mountain Kleiner Feldberg/Taunus (FRG),
 1272 *Atmospheric Research*, Volume 54, Issue 1, 2000, Pages 1-13
- 1273 Mattias-Maser, S., Brinkmann, J., Schneider, W., 1999. The size distribution of marine
 1274 atmospheric aerosol with regard to primary biological aerosol particles over the South
 1275 Atlantic Ocean. *Atmospheric Environment* 33, 3569–3575.
- 1276 Mattias-Maser, S., Jaenicke, R., 1995. The size distribution of primary biological aerosol
 1277 particles with radii > 0.2 μm in an urban/rural influenced region. *Atmospheric Research*
 1278 39, 279–286
- 1279 Mülmenstädt, J., Sourdeval, O., Delanoë, J., and Quaas, J. (2015), Frequency of occurrence
 1280 of rain from liquid-, mixed-, and ice-phase clouds derived from A-Train satellite
 1281 retrievals, *Geophys. Res. Lett.*, 42, 6502– 6509
- 1286 Möhler, O., and Coauthors, 2008: *Heterogeneous ice nucleation activity of bacteria: new*
 1287 *laboratory experiments at simulated cloud conditions.* 1425–1435 pp.
 1288 www.biogeosciences.net/5/1425/2008/.
- 1289 Moisseev, D. N., Lautaportti, S., Tyynela, J., and Lim, S. (2015), Dual-polarization radar
 1290 signatures in snowstorms: Role of snowflake aggregation, *J. Geophys. Res.*
 1291 *Atmos.*, 120, 12644– 12655, doi:10.1002/2015JD023884.
- 1292 Morris, C. E., F. Conen, J. Alex Huffman, V. Phillips, U. Pöschl, and D. C. Sands, 2014:
 1293 Bioprecipitation: A feedback cycle linking Earth history, ecosystem dynamics and land
 1294 use through biological ice nucleators in the atmosphere. *Global Change Biology*, 20,
 1295 341–351, <https://doi.org/10.1111/gcb.12447>.
- 1296 Murray, B. J., D. O'Sullivan, J. D. Atkinson, and M. E. Webb, 2012: Ice nucleation by
 1297 particles immersed in supercooled cloud droplets. *Chem. Soc. Rev.*, 41, 6519–6554,
 1298 <https://doi.org/10.1039/c2cs35200a>.
- 1299 Patade, S., Phillips, V. T. J., Amato, P., Bingemer, H. G., Burrows, S. M., DeMott, P. J.,
 1300 Goncalves, F. L. T., Knopf, D. A., Morris, C. E., Alwmark, C., Artaxo, P., Pöhlker, C.,
 1301 Schrod, J., & Weber, B. (2021). Empirical Formulation for Multiple Groups of Primary
 1302 Biological Ice Nucleating Particles from Field Observations over Amazonia, *Journal of*
 1303 *the Atmospheric Sciences*, 78(7), 2195-2220.

- 1304 Phillips, V. T. J., Donner, L. J., and Garner, S.: Nucleation processes in deep convection
1305 simulated by a cloud-system resolving model with double-moment bulk microphysics, *J.*
1306 *Atmos. Sci.*, **64**, 738– 761, 2007.
- 1307 Phillips, V. T. J., DeMott, P. J., & Andronache, C. (2008). An Empirical Parameterization of
1308 Heterogeneous Ice Nucleation for Multiple Chemical Species of Aerosol, *Journal of the*
1309 *Atmospheric Sciences*, **65**(9), 2757-2783.
- 1310 Phillips, V. T. J., and Coauthors, 2009: Potential impacts from biological aerosols on
1311 ensembles of continental clouds simulated numerically. *Biogeosciences*, **6**, 987–1014,
1312 <https://doi.org/10.5194/bg-6-987-2009>.
- 1313 Phillips, V. T. J., Yano, J., Formenton, M., Iltoviz, E., Kanawade, V., Kudzotsa, I., Sun, J.,
1314 Bansemer, A., Detwiler, A. G., Khain, A., & Tessendorf, S. A. (2017). Ice
1315 Multiplication by Breakup in Ice–Ice Collisions. Part II: Numerical Simulations, *Journal*
1316 *of the Atmospheric Sciences*, **74**(9), 2789-2811.
- 1317 Phillips, V. T. J., Formenton, M., Kanawade, V. P., Karlsson, L. R., Patade, S., Sun, J.,
1318 Barthe, C., Pinty, J., Detwiler, A. G., Lyu, W., & Tessendorf, S. A. (2020). Multiple
1319 Environmental Influences on the Lightning of Cold-Based Continental Cumulonimbus
1320 Clouds. Part I: Description and Validation of Model, *Journal of the Atmospheric*
1321 *Sciences*, **77**(12), 3999-4024
- 1322 Phillips, V. T. J., J. I. Yano, and A. Khain, 2017c: Ice multiplication by breakup in ice-ice
1323 collisions. Part I: Theoretical formulation. *Journal of the Atmospheric Sciences*, **74**,
1324 1705–1719, <https://doi.org/10.1175/JAS-D-16-0224.1>.
- 1325 Phillips, V. T. J., P. J. Demott, C. Andronache, K. A. Pratt, K. A. Prather, R. Subramanian,
1326 and C. Twohy, 2013: Improvements to an empirical parameterization of heterogeneous
1327 ice nucleation and its comparison with observations. *Journal of the Atmospheric*
1328 *Sciences*, **70**, 378–409, <https://doi.org/10.1175/JAS-D-12-080.1>.
- 1329 Phillips, V. T. J., S. Patade, 2021: Multiple Environmental Influences on the Lightning of
1330 Cold-based Continental Convection. Part II: Sensitivity Tests for its Charge Structure
1331 and Land-Ocean Contrast. *Journal of the Atmospheric Sciences*,
1332 <https://doi.org/10.1175/JAS-D-20-0234.1>
- 1333 Phillips, V. T. J., S. Patade, J. Gutierrez, and A. Bansemer, 2018: Secondary ice production
1334 by fragmentation of freezing drops: Formulation and theory. *Journal of the Atmospheric*
1335 *Sciences*, **75**, 3031–3070, <https://doi.org/10.1175/JAS-D-17-0190.1>.
- 1336 Prenni, A. J., and Coauthors, 2013: The impact of rain on ice nuclei populations at a forested
1337 site in Colorado. *Geophysical Research Letters*, **40**, 227–231,
1338 <https://doi.org/10.1029/2012GL053953>.
- 1339 Pörrner, Hans O., et al., 2022: Summary for policymakers. In: Climate change 2022: Impact,
1340 adaptation, and vulnerability: Summary for policy makers: Working group II
1341 Contribution to the sixth assessment report of the Intergovernmental Panel on Climate
1342 Change.

- 1343 Ryzhkov, A., Pinsky, M., Pokrovsky, A., & Khain, A. (2011). Polarimetric Radar
1344 Observation Operator for a Cloud Model with Spectral Microphysics, *Journal of Applied*
1345 *Meteorology and Climatology*, 50(4), 873-894
- 1346 Sahyoun, M., Wex, H., Gosewinkel, U., Šantl-Temkiv, T., Nielsen, N. W., Finster, K.,
1347 Sørensen, J. H., Stratmann, F., and Korsholm, U. S.: On the usage of classical nucleation
1348 theory in quantification of the impact of bacterial INP on weather and climate, *Atmos.*
1349 *Environ.*, 139, 230–240, <https://doi.org/10.1016/j.atmosenv.2016.05.034>, 2016.
- 1350 Sesartic, A., U. Lohmann, and T. Storelvmo, 2012: Bacteria in the ECHAM5-HAM global
1351 climate model. *Atmospheric Chemistry and Physics*, **12**, 8645–8661,
1352 <https://doi.org/10.5194/acp-12-8645-2012>.
- 1353 Sesartic, A., U. Lohmann, and T. Storelvmo, 2013: Modelling the impact of fungal spore ice
1354 nuclei on clouds and precipitation. *Environmental Research Letters*, **8**,
1355 <https://doi.org/10.1088/1748-9326/8/1/014029>.
- 1356 Sinclair, V. A., Moisseev, D., and von Lerber, A. (2016), How dual-polarization radar
1357 observations can be used to verify model representation of secondary ice, *J. Geophys.*
1358 *Res. Atmos.*, 121, 10,954– 10,970, doi:10.1002/2016JD025381.
- 1359 Sotiropoulou, G., Ickes, L., Nenes, A. and Ekman, A.: Ice multiplication from ice–ice
1360 collisions in the high Arctic, 2021b: sensitivity to ice habit, rimed fraction, ice type and
1361 uncertainties in the numerical description of the process, *Atmos. Chem. Phys.*, 21, 9741–
1362 9760, 1313 doi:10.5194/acp-21-9741-2021,
- 1363 Sotiropoulou, G., Vignon, E., Young, G., Morrison, H., O’Shea, S. J., Lachlan-Cope, T.,
1364 Berne, A. and Nenes, A. 2021a: Secondary ice production in summer clouds over the
1365 Antarctic coast: 1308 An underappreciated process in atmospheric models, *Atmos.*
1366 *Chem. Phys.*, 21(2), 755– 1309 771, doi:10.5194/acp-21-755-2021,
- 1367 Spracklen, D. v., and C. L. Heald, 2014: The contribution of fungal spores and bacteria to
1368 regional and global aerosol number and ice nucleation immersion freezing rates.
1369 *Atmospheric Chemistry and Physics*, **14**, 9051–9059, [https://doi.org/10.5194/acp-14-](https://doi.org/10.5194/acp-14-9051-2014)
1370 [9051-2014](https://doi.org/10.5194/acp-14-9051-2014).
- 1371 Szyrmer, W., Zawadzki, I., 1997. Biogenic and anthropogenic sources of ice-forming
1372 nuclei: A review. *Bull. Am. Meteorol. Soc.* 78, 209–228.
- 1373 Tsushima, Y., S. Emori, T.Ogura, et al., 2006: Importance of the mixed-phase cloud
1374 distribution in the control climate for assessing the response of clouds to carbon dioxide
1375 increase: a multi-model study. *Clim Dyn* 27, 113–126 (2006).
1376 <https://doi.org/10.1007/s00382-006-0127-7>.
- 1377 Wilson, T., and Coauthors, 2015: A marine biogenic source of atmospheric ice-nucleating
1378 particles. *Nature*, 525, 234–238, <https://doi.org/10.1038/nature14986>.
- 1379 Xie, S., Y. Zhang, S. E. Giangrande, M. P. Jensen, R. McCoy, and M. Zhang, 2014:
1380 Interactions between cumulus convection and its environment as revealed by the MC3E
1381 sounding array. *Journal of Geophysical Research*, **119**, 11,784-11,808,
1382 <https://doi.org/10.1002/2014JD022011>.

1383 Zhao, X., & Liu, X. (2021). Global importance of secondary ice production. *Geophysical*
1384 *Research Letters*, 48, e2021GL092581. <https://doi.org/10.1029/2021GL092581>

1385 Zuidema, P., E. R. Westwater, C. Fairall, and D. Hazen, 2005: Ship-based liquid water path
1386 estimates in marine stratocumulus. *J. Geophys. Res.*, **110**, D20206,
1387 doi:10.1029/2005JD005833.

1388

1389

1390